KeAi
CHINESE ROOTS
GLOBAL IMPACT

Available online at www.keaipublishing.com/en/journals/journal-of-magnesium-and-alloys/

ScienceDirect

Journal of Magnesium and Alloys 13 (2025) 3490–3523

www.elsevier.com/locate/jma

Review

The potential of deformable titanium reinforced magnesium-matrix composites: A review of preparation, characterization, and performance evaluation ☆

Yitao Wang [a], Jianbo Li [a,b,*], Huan Luo [a], Weizhang Wang [a], Daiyi Deng [a], Jianwei Chen [a], Xianhua Chen [a,*], Kaihong Zheng [c], Fusheng Pan [a]

[a] College of Materials Science and Engineering, Chongqing University, Chongqing 400044, China
[b] Chongqing Institute of New Energy Storage Materials and Equipment, Chongqing 401135, China
[c] Institute of New Materials, Guangdong Academy of Sciences, Guangzhou 510650, China

Received 8 April 2025; received in revised form 18 June 2025; accepted 28 June 2025
Available online 29 July 2025

Abstract

Magnesium matrix composites (MMCs) combine exceptional low density, high specific strength, and stiffness, positioning them as critical materials for aerospace, automotive, and electronics industries. This review highlights recent progress in the fabrication of Ti-Mg composites and analyzes the mechanisms behind their enhanced mechanical properties. A key focus is the interfacial deformation incompatibility between Ti and Mg phases, which generates strain gradients and promotes the accumulation of geometrically necessary dislocations (GNDs) at the interface. This process not only improves strain hardening and ductility but also reveals the need for advanced micromechanical models to capture the plastic behavior of both phases. The review critically examines the impact of different Mg matrix types (AZ, AM, VW series) and the role of interfacial product morphology and size on bonding and overall performance. Furthermore, Ti reinforcement endows the composites with superior wear resistance and thermal conductivity, indicating broad application potential.

Keywords: Magnesium matrix composites; Deformable Ti reinforcement; Mechanical properties.

1. Introduction

Magnesium (Mg) and its alloys (e.g., Mg-Al-Zn, Mg-Ca-Zn, Mg-Gd-Zn and Mg-Y-Zn) are considered excellent choices for lightweight structural components due to their low density and abundant availability [1–5]. Their application across industries like aerospace, transportation, and defense has the potential to substantially lower CO_2 emissions, contributing to global efforts aimed at energy conservation and emission reduction [6,7]. Despite their advantages, Mg alloys face challenges regarding their mechanical properties. To improve the mechanical properties of Mg alloys, various strategies have been explored in recent years. Microstructural engineering, such as texture modification and control of grain size and distribution, contributes to higher yield and ultimate tensile strengths [8,9]. Severe plastic deformation techniques, including and high-pressure torsion, significantly refine grains and increase dislocation density, thus enhancing mechanical properties [10–12]. Additionally, introducing appropriate alloying elements (e.g., Zn, Zr, Gd, and Y) can enhance phase stability and facilitate both solid solution and precipitation strengthening, leading to finer, more uniform grain structures and improved mechanical properties [13,14]. Current methods for alloying Mg struggle to improve their tensile strength beyond 550 MPa while also maintaining an elongation of 8%, which limits their suitability for demanding applications [15].

☆ Peer review under the responsibility of Chongqing University.

* Corresponding authors at: College of Materials Science and Engineering, Chongqing University, Chongqing 400044, China.
E-mail addresses: lijianbo1202@cqu.edu.cn (J. Li), xhchen@cqu.edu.cn (X. Chen).

https://doi.org/10.1016/j.jma.2025.06.027

Table 1
The summary of various Ti reinforcements and its mechanical properties.

	E (GPa)	YS (MPa)	UTS (MPa)	EL (%)	Hardness (HV)
Pure Ti [35,36]	105	160–214	290–365	42–54	120–160
Ti6Al4V [35,37–39]	110–124	760–880	830–1025	12–16	340–370
TiNi [40–42]	20–108	195–690	850	25–50	190

E-Elastic modulus; YS-Yield strength; UTS-Ultimate tensile strength; EL-Strain failure.

To address these challenges, magnesium-matrix composites (MMCs) have been developed. This approach strengthens the Mg matrix by incorporating tougher materials such as ceramics, metals, and intermetallic compounds, enhancing the alloys' mechanical performance at both room and elevated temperatures [16–18].

In the past decades, much of the focus in evolutionary studies has been on selecting reinforcements, particularly robust ceramic reinforcements, such as SiC, TiC, B_4C, Al_2O_3, and TiB_2, to enhance the yield strength of the composites [19–26]. However, the addition of ceramic reinforcements in MMCs significantly compromises their plasticity due to reinforcements' brittle performance and inability to deform synergistically with the matrix. This mismatch leads to stress concentration and premature crack formation. In contrast to ceramics, metals and intermetallic compounds with high Young's modulus and superior plasticity are increasingly regarded as ideal reinforcements for MMCs. Common metallic reinforcements include titanium (Ti), copper (Cu), nickel (Ni), Al_3Ti, TiNi, and Al_3Fe, respectively [27–32]. Among these, Ti and its alloys have the advantage of better load transfer and coordinated deformation by virtue of better wettability with Mg [16,33]. In cast materials, Mg-Ti intermetallic bonds form a stable, coherent connection without observable microporosity at the interface. Additionally, the lattice constant mismatch is significantly lower than the critical threshold required for the formation of coherent interfaces [34]. The most commonly used titanium-based reinforcements include Ti, Ti_6Al_4V (TC4), and TiNi memory alloy, whose mechanical properties are outlined in Table 1. Pure Ti generally shows moderate modulus and strength but exhibits excellent ductility, making it suitable as a deformable reinforcement phase, especially for enhancing the ductility and toughness of MMCs. In contrast, Ti6Al4V provides much higher strength and hardness but lower ductility, making it desirable for applications demanding increased mechanical strength and wear resistance in MMCs. TiNi displays a wide range of properties due to its compositional and structural variabilities; in Mg matrix composites, it is used not only for its moderate strength and elasticity, but also for imparting functional characteristics such as shape memory, superelasticity, self-healing, and damping. Ti-reinforced MMCs are garnering increasing attention in various sectors due to their exceptional combination of mechanical properties, including high strength, toughness, and fatigue resistance, without a significant loss in plasticity for MMCs.

A search of the Web of Science (WoS) Core Collection database was performed on June 1, 2025, targeting publications from the last 5 years with "magnesium matrix composites" or "Mg matrix composite" as the topic. To further refine the scope, an advanced query was used to identify publications specifically focusing on composites reinforced with "Ti, TC4, TiNi, pure titanium, or Ti6Al4V". As illustrated in Fig. 1, the green bars represent the total number of MMC publications each year, while the brown bars indicate the proportion of Ti-reinforced MMCs. It is evident that the total number of MMC publications has exhibited a consistent upward trend, increasing from 532 in 2020 to 969 in 2022, with a slight decrease to 886 in 2024. Notably, the proportion of Ti-reinforced MMCs among the total MMC publications has shown a significant rise over the same period, with the percentage increasing from 0.94% in 2020 to 5.64% in 2024. This marked growth reflects escalating research interest in Ti-reinforced MMCs, demonstrating that Ti-reinforced magnesium matrix composites are rapidly emerging as a major focus and hotspot within the field of materials science and engineering in the past 5 years.

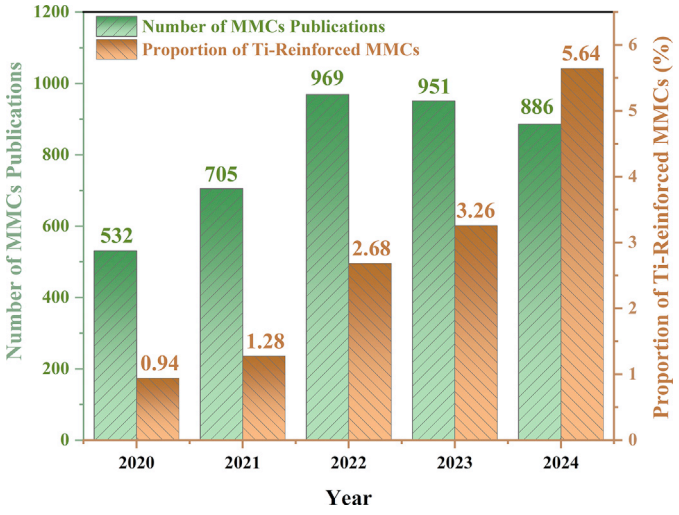

Fig. 1. Published MMCs-related papers in the past 5 years in the Web of Science (WoS) Core Collection database (searched on June 1, 2025).

However, the fabrication, characterization, and performance assessment of these composites remain challenging due to the complex interactions between the Mg and Ti components. Successfully preparing these materials demands careful attention to the properties of both elements, while accurate characterization and performance evaluation require a comprehensive understanding of the microstructure and fac-

tors such as grain size, interfacial products, and deformation mechanisms that affect their behavior.

In this paper, the current developments in the preparation, characterization, and performance evaluation of deformable Ti-reinforced MMCs are comprehensively reviewed. In contrast to prior reviews that have mainly concentrated on synthesis techniques and general mechanical properties, this work places particular emphasis on the deformation incompatibility at the Ti-Mg interface and its influence on strain hardening and ductility. The review systematically covers diverse fabrication methods—including casting, friction stir processing, and powder metallurgy—as well as advanced characterization approaches such as in-situ SEM and digital image correlation, which are instrumental in elucidating the microstructure, wettability, tensile and compressive behaviors, tribological performance, and constitutive relations of Ti-Mg composites. Furthermore, this article critically examines the current limitations of micromechanical modeling, particularly in capturing the concurrent plasticity of both constituent phases, and highlights the significant impact of interfacial product morphology on both mechanical and functional properties of the composites. Accordingly, this review paper also provides insights into the future directions of research and development trajectories, including the exploration of novel preparation methods, the advancement of characterization techniques, and the assessment of composite performance under various loading conditions and environmental factors.

2. Processing methods of Ti-Mg composites

To date, several methods have been established for the fabrication of Mg matrix composites [43]. These fabrication methods can be broadly classified into two categories depending on the state of the matrix during the preparation process: solid-liquid composite preparation and solid-state.

2.1. Solid-liquid compound preparation

Solid-liquid state preparation is suitable for making Ti-Mg composites in large shapes and quantities, and it is also a relatively inexpensive process. It involves the direct dispersion of the Ti reinforcements into the liquid Mg matrix and the subsequent solidification. The casting process is one of the less expensive fabricating methods widely operated to increase materials' strength and deformation ability [44,45].

2.1.1. Semi-solid stir casting

Semi-solid stir casting (SSSC) is a commonly employed technique to fabricate MMCs reinforced with pure Ti or Ti alloy particles. As depicted in Fig. 2a, the application of SSSC is usually combined with ultrasonic vibration. In the SSSC-assisted ultrasonic vibration process, the matrix alloy is firstly melted in CO_2+SF_6 protective atmosphere and then cooled to a semi-solid state. Subsequently, pre-heated reinforcement particles are added to the semi-solid alloy and stirred. After stirring, the mixed melt is reheated and subjected to ultrasonic vibration. Finally, the melt is poured into a steel mold and solidified to form composite ingots [46]. The SSSC method offers several advantages for MMC production, including high production efficiency, cost-effectiveness, simplicity, and flexibility. Additionally, it prevents the formation of coarse dendritic crystals that often occur in traditional casting methods and enables the macroscopic dispersion of particulate reinforcements [47,48]. In recent literature, numerous focused on preparing Mg composites using SSSC-assisted ultrasonic vibration. For example, Pu et al. [49] successfully fabricated a Ti particle-reinforced VW84 composite using this technique, achieving a uniform distribution of Ti particles.

2.1.2. Solid-liquid compound casting

Solid-liquid compound casting (SLCC) represents a casting methodology where liquid and solid metals directly interact. During this process, atomic diffusion takes place at the liquid-solid interface, facilitating the formation of uniformly distributed intermetallic compounds within the matrix. This interaction promotes strong bonding and leads to the synthesis of composite materials [50–53]. The bonding properties of solid-liquid composite castings are largely determined by the interfacial reaction products. As shown in Fig. 2b, Wen et al. [54] successfully produced Ni-coated TC4 reinforced AZ91 bimetallic materials at pouring temperatures of 690, 720, and 750 °C. The results revealed that increasing the casting temperature from 690 °C to 720 °C caused a gradual enlargement of the interfacial reaction zone. In addition, they also investigated the surface coating of solid TC4 rods with different thicknesses of Cu layer. The increased Cu layer thickness induced a microstructural evolution at the interface [55].

2.1.3. Pressureless infiltration

Pressureless infiltration (PI) is a method for fabricating composites that relies on capillary forces to enable molten metal to spontaneously penetrate a porous preform. This process is highly uniform and results in dense composites with minimal porosity. The volume fraction of the reinforcement phase can be precisely controlled by adjusting the porosity of the preform, making PI an ideal technique for producing metal matrix composites with high reinforcement content. Fig. 2c provides a simplified schematic representation of the PI technique, showing the solid metallic alloy before melting, floowed by the spontaneous infiltration of the liquid metal. For example, Li et al. [56] successfully fabricated a dense Ti/Mg composite using PI method driven by capillary pressure, avoiding significant shrinkage. Additionlly, Han et al. [57] developed Ti-Mg composites through PI technonlegy, where pure Mg melt was infiltrated into 3D printed pure Ti scaffolds, as illustrated in Fig. 2d. The resulting composites exhibited a unique microstructural characteristic by robust interfacial bonding between Ti and Mg, without intermediate transition layers either noticeable elemental interdiffusion. The microstructure was mainly composed of separate Ti and Mg phases, each maintaining its structural integrity without the formation of additional phases or solid solution structures.

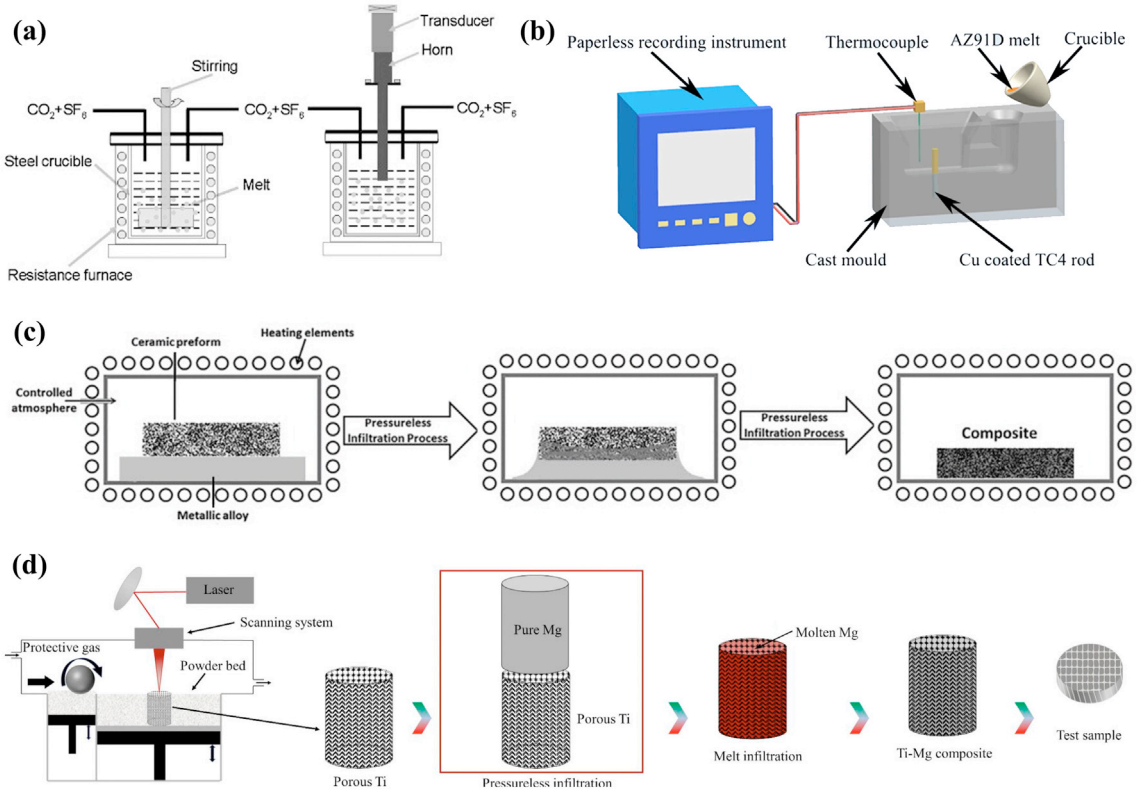

Fig. 2. Schematic diagrams of experimental setups: (a) semi-solid stirring with ultrasonic vibration [46]; (b) compound casting [54,55]; (c) pressureless infiltration [58]; (d) 3D printing and pressureless infiltration [57].

2.2. Solid-state preparation

In contrast to liquid-state fabrication, the solid-state preparation route generally takes longer and results in more limited shapes for the produced composites. However, one key advantage of solid-state processing is that the Ti-Mg composite reinforcements maintain exceptional uniformity in their distribution. Fig. 3 illustrates a schematic diagram of various solid-state methods for fabricating MMCs. The following section highlights several commonly used solid-state techniques for producing Ti-Mg composites.

2.2.1. Powder metallurgy

The powder metallurgy (PM) technique is an effective method for simultaneously obtaining high-yield stress and plasticity, thanks to its ability to evenly distribute the reinforcement within the matrix [59,60]. Typically, the route of PM involves three primary steps: powder mixing, sintering, and extrusion, as shown in Fig. 3a. One of the key characteristics of PM is the thorough mixing of powders during the ball milling stage [61,62]. Additionally, the sintering temperature remains below the melting point of Mg, minimizing the interfacial reaction between Ti particles and the Mg matrix, which results in a relatively uniform distribution of Ti particles in the MMCs [63]. Tang et al. [64] investigated the preparation of pure AZ91 and a 5Ti/ AZ91 composite using powder metallurgy followed by extrusion. They found that non-homogeneous deformation of Ti particles and α-Mg matrix produces additional heterogeneous deformation-induced (HDI) strengthening to enhance the strength of Ti_p/AZ91, which improved the composite's strength. Wang et al. [65] prepared TC4 particles reinforced Mg-Gd-Zn-Zr alloy matrix composites (TC4/GZ151K) by same methods and reported that TC4 incorporation weaken the texture and refine the grain size of matrix. furthermore, the deformable TC4 particles co-deformed with the matrix, which helped to inhibit crack initiation, thereby improving the plasticity of the composites.

2.2.2. Hot-pressing sintering

Hot-pressing sintering (HPS) is a technique where raw materials are subjected to high temperature and pressure, resulting in densification and the fixation of shape [62]. This method enables the simultaneous action of pressure-assisted plastic deformation and diffusion, which together promote densification and strengthen the interfacial bond between the reinforcement and the matrix, as illustrated in Fig. 3b. Cai et al. [66] fabricated Mg-Ti composites through a novel one-step high-pressure sintering method. By sintering low-melting-point Mg and high-melting-point titanium simultaneously, they achieved a fully dense microstructure in the composite material. In another study, Mizuuchi

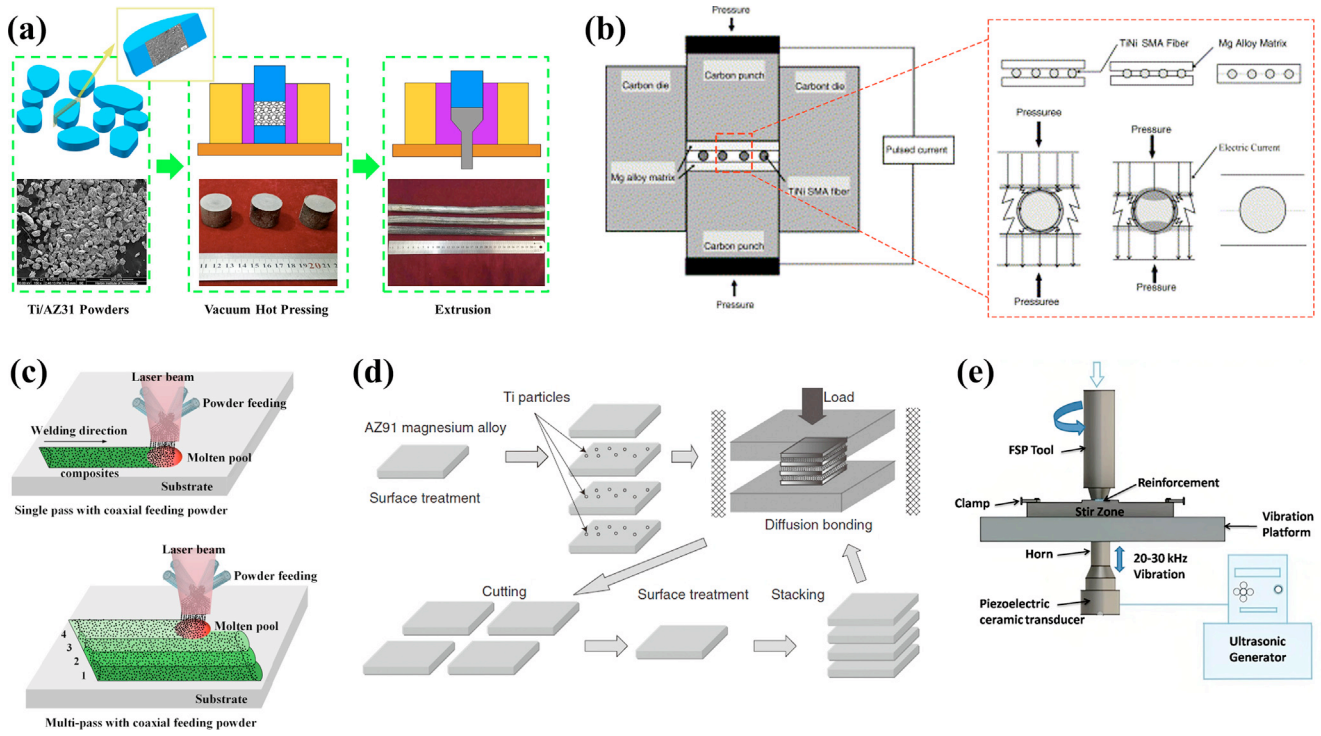

Fig. 3. Schematic of solid-state preparation methods: (a) powder metallurgy [81]; (b) pulsed current hot pressing [67]; (c) laser melt injection [76]; (d) accumulative diffusion bonding [70]; (e) friction stir processing with/without ultrasonic vibration [51].

et al. [67] developed pulsed current hot pressing (PCHP) technique to fabricate MMCs reinforced with continuous TiNi shape memory alloy (SMA) fibers. By sandwiching TiNi SMA fibers between AZ31 plates under pulsed current, the process enhances interfacial bonding via in-situ surface purification and localized Joule heating at fiber-matrix interfaces. Compared to conventional HPS, PCHP process achieves better surface purification and activation of fibers and plates, resulting in high-quality laminated composite [68,69]. Furthermore, PCHP demonstrates a 30%–50% reduction in processing-induced contamination compared to spark plasma sintering (SPS), because of the low surface-to-volume ratio in the plates. This advantage positions PCHP as a preferred method for oxygen-sensitive Mg-Ti composite systems.

2.2.3. Accumulative diffusion bonding

Accumulative diffusion bonding (ADB) is particularly well-suited for preparation of bionic layered non-homogeneous composites, making it ideal for large-scale structural materials due to its simple hot pressing procedure [70]. As illustrated in Fig. 3c, the ADB method is used to manufacture Ti particle-reinforced MMCs, eschewing the need for either Mg melts or powders in the process.

The main advantages of ADB technology in composite material fabrication include its ability to achieve effective bonding at lower temperatures, thereby avoiding the interfacial reaction issues typically associated with traditional melting techniques [71,72]. Kitazono et al. [73] revealed that the method also promotes significant grain refinement and random texture development through multiple cumulative deformations. Additionally, ADB enables the combination of different material types, allowing the creation of laminated composites with superior performance. It offers excellent process control, enabling precise regulation of interfacial structures and properties [74]. Furthermore, ADB can produce large-sized plates with high interfacial bonding strength and excellent internal quality [75], making it particularly well-suited for the preparation of metal matrix composites and functional gradient materials.

2.2.4. Laser melt injection

Laser melt injection (LMI) is a technique that creates a localized melt pool on the surface of the matrix by irradiating it with a laser beam, while simultaneously introducing reinforcing phase particles. This enables in-situ composite formation during rapid solidification. LMI allows for the development of continuous, defect-free composite layers on the substrate surface. The laser's characteristic rapid thermal cycling fosters the formation of refined microstructures at the interface between the reinforcing phase and the matrix, establishing robust metallurgical bonding. This process not only improves interfacial adhesion strength but also facilitates selective reinforcement of specific areas to address localized performance requirements [76,77]. Despite the processing challenges posed by Mg alloys, including their susceptibility to porosity and defects due to their unique physical-chemical properties, researchers have successfully applied laser melt injection to

produce TiP/Mg-RE composites [76]. In this process, as depicted in Fig. 3d, Ti particles from four channels converge at the coaxial position of the laser beam before entering the molten pool. The effectiveness of process was closely monitored through continuous real-time observation of melt pool's stability during the bonding process, with high-speed camera imaging used to assess the quality of the metallurgical bonding.

2.2.5. Friction stir process

Friction stir processing (FSP), as depicted in Fig. 3e, offers distinct advantages in fabrication of MMCs, particularly through its capacity to mix and bond materials effectively in the solid state [78,79]. The mechanical stirring action during FSP promotes a uniform distribution of reinforcement phases within the matrix, avoiding the interfacial reactions and reinforcement clustering issues commonly associated with traditional melt-based fabrication methods [80]. Dinaharan et al. [79] employed stirring and friction techniques to prepare of Ti/AZ31B composites. Their results indicated that a lower feed rate (30 mm/min) was beneficial for generating frictional heat and mechanical agitation, which enhanced the uniform distribution of particles. Additionally, increasing the number of stirring passes (4–5 passes) significantly improve particle distribution. Kumar et al. [51] fabricated TiC/AZ31 composite via FSP without and with ultrasonic vibration (FSVP). Their finding revealed that FSVP processing helped mitigate flow-related defects, such as void formation and tunneling effects. More crucially, the enhanced material flow characteristics and increased fluidity achieved through FSVP contributed to a more uniform distribution of reinforcement particles within the matrix, resulting in notable improvements in the composite's properties.

2.3. Summary of processing methods for Ti-Mg composites

Table 2 systematically compares various processing routes for Ti-Mg composites according to their classification in Section 2.1 and 2.2, including both solid-liquid and solid-state preparation techniques. Among the solid-liquid compound preparation methods, semi-solid stir casting, solid-liquid compound casting, and pressureless infiltration are highlighted for their feasibility in large-scale production and relative simplicity. However, these methods often encounter challenges such as limited uniformity in Ti particle distribution, restricted Ti content, and the formation of brittle interfacial phases. In contrast, solid-state preparation methods—including powder metallurgy, hot-pressing sintering, accumulative diffusion bonding, laser melt injection, and friction stir processing—provide superior control over microstructure, interface integrity, and the uniformity of Ti dispersion. As detailed in Table 2, powder metallurgy and hot pressing offer notable improvements in mechanical properties but require rigorous process conditions. Advanced approaches such as accumulative diffusion bonding and laser melt injection enable the fabrication of layered architectures and tailored interfacial characteristics, while friction stir processing supports localized reinforcement and gradient structures. Overall, each technique presents a unique balance of process complexity, interface quality, and attainable composite properties, and the optimal choice depends on the specific structural and functional requirements of the targeted applications.

3. Microstructural characterization

3.1. Wetting behavior of Mg-Ti and its composites

The wetting behavior of composite material refers to its ability to adhere effectively to the matrix material at the reinforcement surface [82]. This property is essential for ensuring proper load transfer and plays a critical role in achieving optimal mechanical properties and performance in composite materials. The wetting angle serves as a measure to quantify the wetting behavior of a composite material, with a smaller wetting angle indicating better wetting and stronger bonding, which in turn leads to enhanced mechanical properties [83,84]. As illustrated in Fig. 4, the wettability of pure Ti by molten pure Mg droplets was evaluated at 1073 K. The true contact angle between Mg and the Ti after 180 s was found to be ∼31°, significantly lower than the 110° contact angle observed with TiC substrates [85,86].

Fig. 5 demonstrates the variations in the contact angle with time for molten Mg droplets on the various substrate surfaces. The values of contact angles under the same conditions are indicated by the red crosshairs. Considering this situation, the wetting angle typically ranges from 40°–60° when ceramic (e.g., SiC, TiC, and B_4C) is used as substrate. Under identical conditions, 180 s and 1073 K, Ti substrate exhibits the lowest wetting angle with molten Mg, as shown in Fig. 5(a), making Ti an ideal candidate for composite materials where Mg serves as the matrix. This favorable wetting behavior translates into the optimal bonding properties between the two materials. Further improvement in wettability can be achieved by increasing the content of Ti-based reinforcing particles within the Mg matrix. As illustrated in Fig. 6, Mahmood et al. [87] studied the wetting behavior of nano-NiTi reinforced Mg-3Zn-0.5Ag composite. The research clearly shows that the contact angle has slightly decreased as the NiTi content increased, indicating enhanced wettability for the Mg-Ti composites. This trend demonstrates that in addition to selecting suitable substrates like Ti to improve MMCs wettability (as shown in Fig. 5), tailoring the amount of Ti reinforcements (as in Fig. 6) is an effective strategy to achieve even stronger interfacial bonding, which is crucial for advancing the performance and application range of Mg-Ti composites, especially in demanding fields such as biomaterials.

3.2. Interfacial characterization of Ti-Mg composites

As demonstrated in previous studies, the choice of reinforcements is pivotal in the fabrication of composites, as it influences the wetting behavior of the liquid matrix and the strength of the matrix/reinforcement bond. Beyond interfacial wettability, slight interfacial reactions are also crucial factors

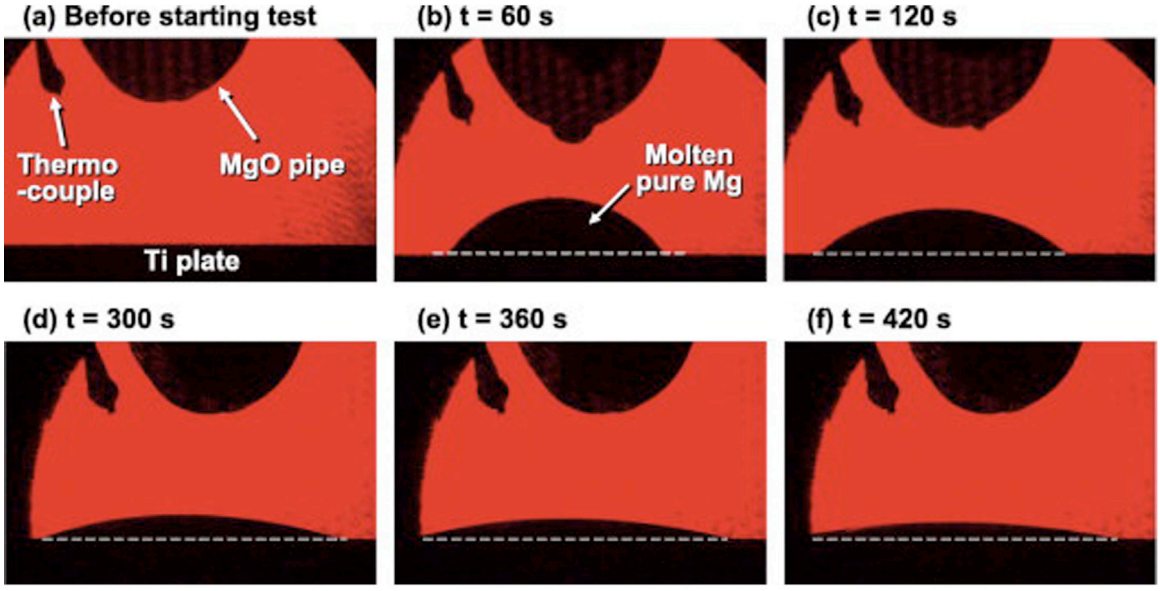

Fig. 4. Photos showing morphological changes of pure Mg molten droplet on pure Ti substrate at 1073 K in the sessile drop test [85].

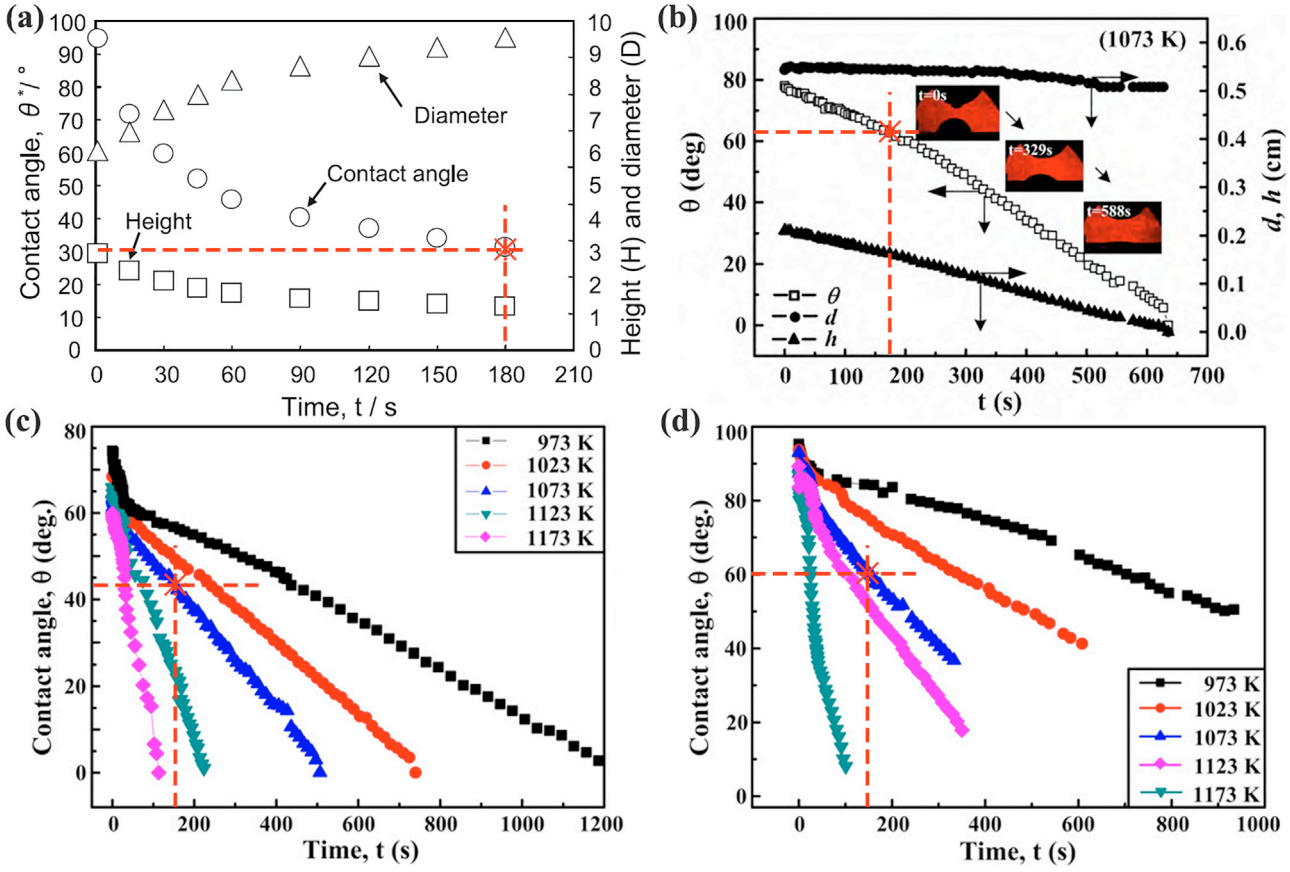

Fig. 5. Variations in the contact angle with time for molten Mg drops on the various surfaces. (a) Pure Ti [85], (b) SiC [88], (c) TiC [89], (d) B_4C [89]. The value of contact angles under the same condition was indicated by rod forks.

Table 2
The summary of processing methods for Ti-Mg composites.

Category	Process method	Advantages	Limitations
Solid-liquid compound preparation	Semi-solid stir casting	Simple process, suitable for industrial production and large-size rod/block samples.	Ti particles tend to settle/agglomerate, limited Ti addition (2%–3%).
	Solid-liquid compound casting	Enhanced interfacial bonding, capability for complex shapes, favorable for formation of thick interfacial transition layers.	Narrow process window, control challenges, formation of brittle Al-Ti reaction products, inhomogeneous Ti distribution.
	Pressureless infiltration	High Ti fraction and uniform distribution.	Template preparation is difficult, strict requirements for preform quality; limited ductility improvement with increased Ti.
Solid-state preparation	Powder metallurgy	Precise Ti content and distribution, easy to achieve nanoscale, minor interface reactions.	Requires high temperature and high pressure, susceptible to porosity/agglomeration; densification must be strictly controlled.
	Hot-pressing sintering	Excellent densification and bonding, suitable for multi-component composites; applicable to complex shapes and multilayers.	High energy consumption, limited by raw material and part dimensions; precise sintering control required.
	Accumulative diffusion bonding	Uniform Ti particle distribution, near-net shaping; controlled interface reaction, low impurity level.	Equipment demanding, high cost under inert atmosphere.
	Laser melt injection	Precise control of local structure/interface and gradient functional reinforcement achievable.	Equipment is expensive, narrow process window, heat-affected zone must be carefully managed.
	Friction stir process	Localized reinforcement, suitable for functional zoning.	Challenging to achieve large-area uniformity, high Ti does not always mean better performance, relatively high cost.

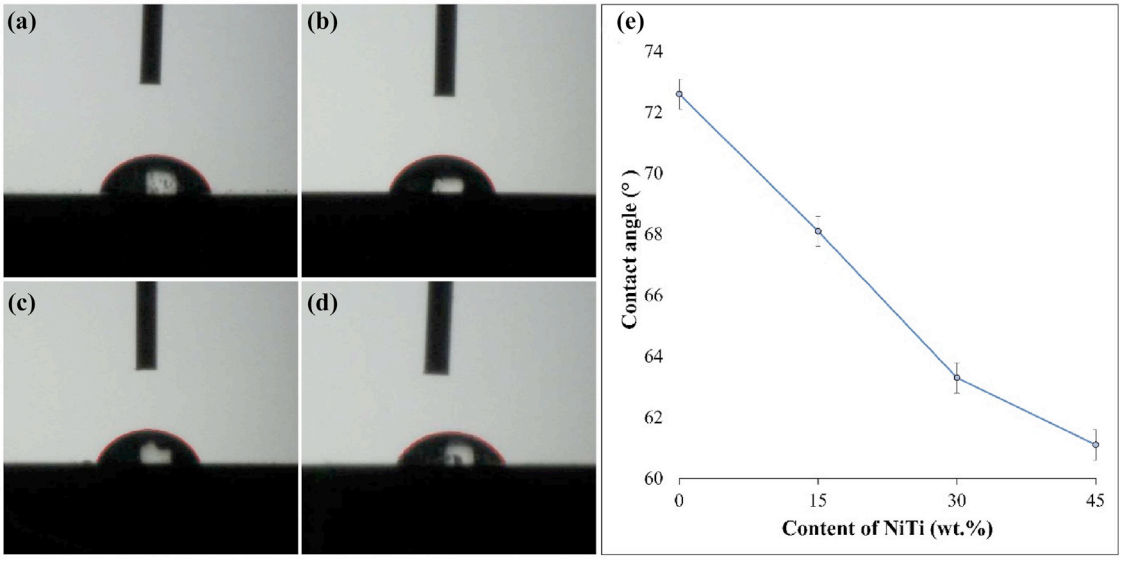

Fig. 6. Water contact angles for matrix and NiTi-reinforced composites (15%, 30%, 45%), and summary of results [87].

that affect the interface properties of the interface [90,91]. Katarzyna [34] summarized the various types of interfaces found in metal matrix composites, as shown in Fig. 7. For metal matrix composites, both the chemical composition of the matrix and the selection of reinforcement type plays a significant role in determining the feasibility of achieving the desired structure. In some cases, specific combinations of these factors may hinder the production of composites with the required properties. This section reviews Mg alloy series reinforced with various Ti reinforcements, each exhibiting

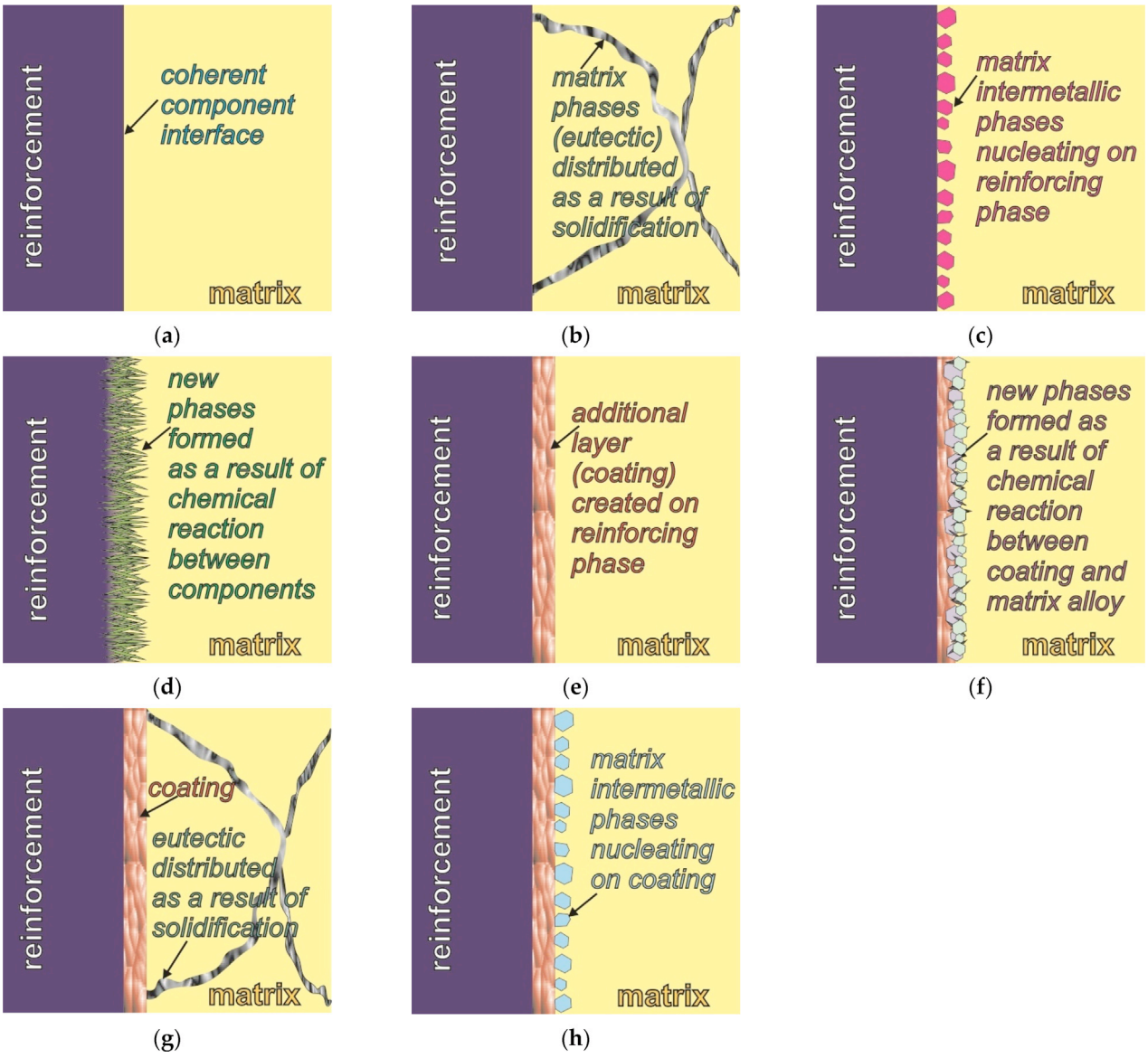

Fig. 7. Scheme of interface types in metal matrix composites: (a) coherent interface; (b) eutectics at interface on solidification; (c) intermetallics nucleated at reinforcement; (d) reaction-formed phases at interface; (e) pre-applied coating on reinforcement; (f) reaction phases from matrix/coating; (g) eutectics distributed during solidification; (h) matrix phases nucleated on coating [34].

different interfacial microstructure, with the goal of providing insights for the development of high-performance Ti-Mg composites.

3.2.1. Mg-Al-Zn series matrix alloy

In the Ti/Mg-Al-Zn system composites, a summary of the interfacial characteristics is displayed in Fig. 8. The interface between Ti and Mg, illustrated in Fig. 8a, demonstrates a permanent and coherent bond, without the presence of microporosity observed at the Ti/Mg interfacial zone [53]. As well, the (10–11) Mg plane and (10–10) Ti plane are inclined at an angle of 12°. Generally, Ti and Mg elements do not react at the interface, resulting in the absence of chemical bonding between the reinforcing phase and the matrix, which leads to weak interfacial bonding. In contrast, Ti element can react with the element Al in AZ series Mg alloys, forming different TiAl compounds. While the mechanism for Ti-Al reaction is still under investigation, it is known that the reaction between pure Ti and Al is diffusion-controlled, involving several intermediate phases, such as $TiAl_2$ and $TiAl_3$, etc. The reaction of Ti element and Al element is accomplished in the following steps:

$$6Al+6Ti \rightarrow 2TiAl_3+4Ti;$$

$$2TiAl_3+4Ti \rightarrow Ti_3Al+TiAl+2TiAl_2;$$

$$Ti_3Al+TiAl+2TiAl_2 \rightarrow 6TiAl;$$

As illustrated in Fig. 8$b_{1\text{-}4}$, the high-resolution TEM (HRTEM) results of the Ti/Mg interface in Ti/Mg-Al-

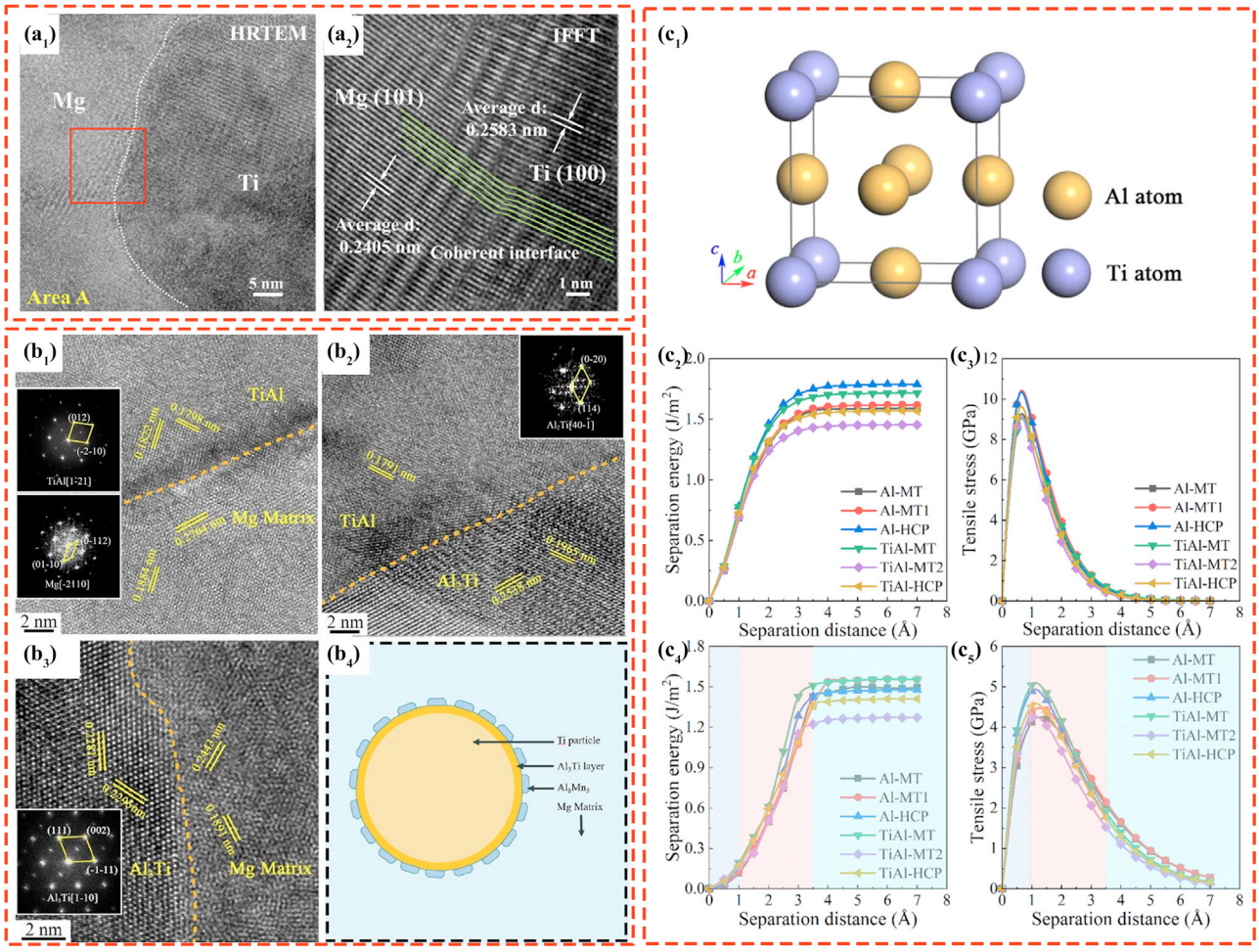

Fig. 8. TEM images and interface analysis of Ti/Mg composite: (a_1) HRTEM of Ti/Mg-9Al-Zn-0.3Mn interface, (a_2) IEEF of red region [93]; interfacial structure in 6 wt.%Ti/AZ31 composite: (b_1) TiAl/Mg interface, (b_2) TiAl/Al_2Ti interface [94], (b_3) Al_3Ti/Mg interface, and (b_4) schematic of Ti particle in Mg matrix [95]; (c_1-c_5) separation energy and tensile stress vs separation distance of Mg(10–10)/Al_3Ti(001) [92].

Zn series composites confirm the presence of the TiAl, $TiAl_2$, and $TiAl_3$ intermetallic compounds. The formation of semi-coherent TiAl/Mg interface ($(0–112)_{Mg}//(012)_{TiAl}$, $[-2110]_{Mg}//[1–21]_{TiAl}$) between Ti reinforcement and Mg matrix, along with in-situ synthesized $TiAl_2$ particle nanoparticles, results in the creation of a semi-coherent $TiAl_2$/Mg interface ($(10–11)_{Mg}//(114)_{TiAl2}$, $[-2110]_{Mg}//[40–1]_{TiAl2}$). The in-situ synthetization significantly improves the atomic bonding between Ti particles and Mg matrix, thereby improving the interfacial bonding of the composites. In the Ti-Al system, it is well established that $TiAl_3$ has the lowest activation energy, facilitating its formation early in the reaction. As the reaction progresses, the Al element form $TiAl_3$ diffuse into the Ti matrix. The first-principles calculations of the bonding strength, energetics, and fracture mechanism of the Mg(10–10)/$TiAl_3$(001) interfaces, reported by Bao et al. [92]. Their results imply that fracture initiation occurs within the bulk Mg interior. Upon fracture, cracks preferentially generate inside the Mg matrix, while in-suit $TiAl_3$ compounds positively enhances the composite's fracture strength, as shown in Fig. 8c_{1-5}.

In addition to TiAl compounds, other intermetallic compounds found in Ti-Mg composites are also present in Ti/AZ composites. Fig. 9 illustrates formation of the Al_8Mn_5, and $Mg_{21}(Zn, Al)_{17}$ intermetallic-compound layer between TC4/Mg, thus significantly increasing the ultimate tensile strength, even at a thin size. Two types of bonding play a critical role in strengthening the interface: coherent interfacial bonding between $TiAl_3$/$Mg_{21}(Zn, Al)_{17}$ arises from strong atomic lattice alignment, characterized by low lattice mismatch. This minimizes interfacial energy, enabling efficient stress transfer across the interface; semi-coherent interfacial bonding between $TiAl_3$/$Mg_{21}(Zn, Al)_{17}$/Mg introduces periodic arrays of interfacial dislocations that accommodate local lattice misfit. These dislocations help to relieve strain while maintaining interfacial stability. Robust bonding enhances the efficiency of load transfer from the Mg matrix to the TC4 particles, enabling the composite to resist higher stresses. Con-

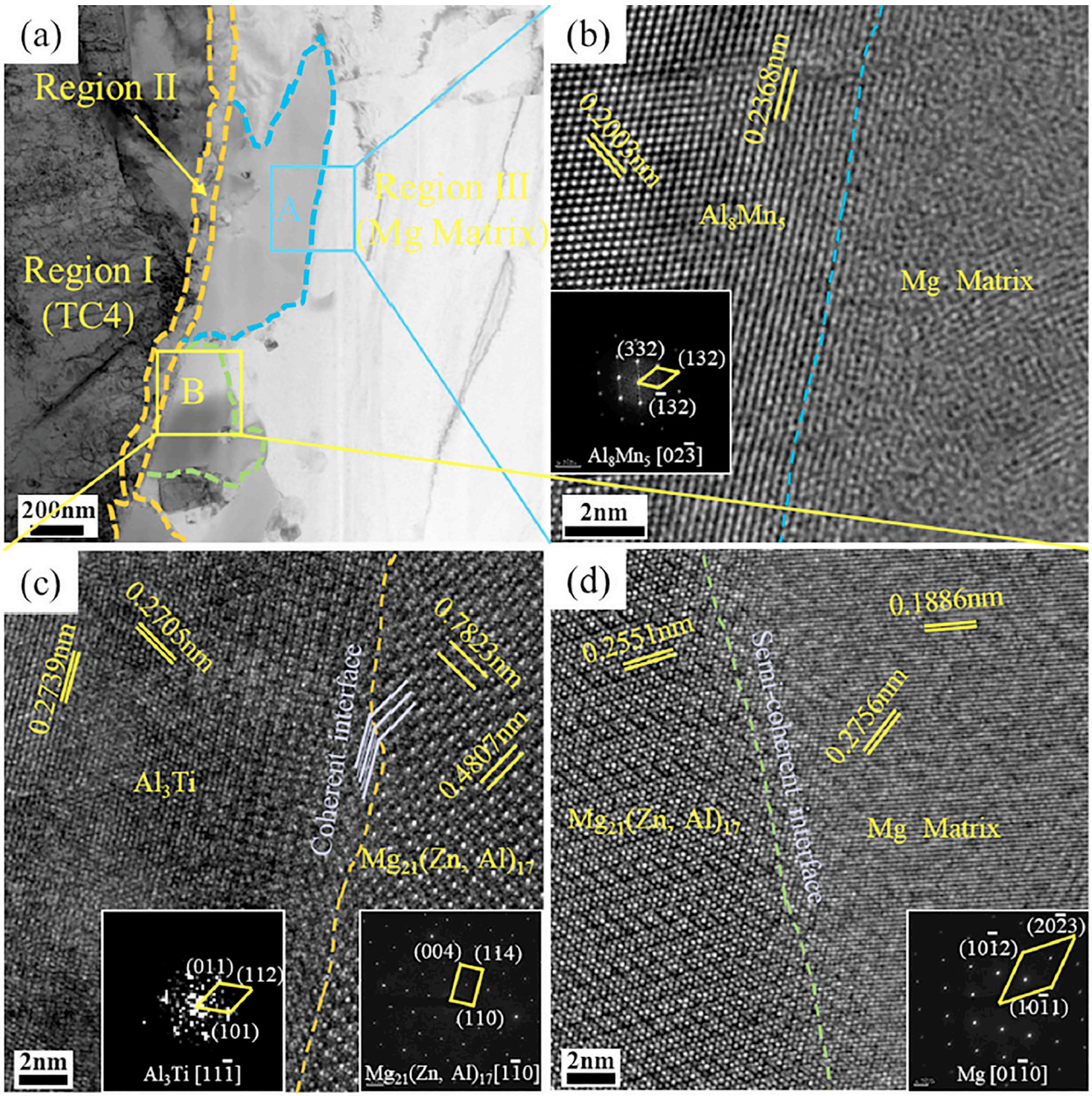

Fig. 9. Interface structure of AZ91–5 wt.% TC4 composite: (a) TEM image, (b) Al_8Mn_5/Mg interface with FFT patterns of Al_8Mn_5; (c) Al_3Ti/$Mg_{21}(Zn, Al)_{17}$ interface with FFT patterns of Al_3Ti and $Mg_{21}(Zn, Al)_{17}$, (d) $Mg_{21}(Zn, Al)_{17}$ interface with FFT pattern of Mg matrix [96].

sequently, both the strength and ductility of the composite are improved, with the coherent zones supporting stress transfer and the semi-coherent regions mitigating stress concentration through controlled strain accommodation.

Li et al. [97] operated HPS method to fabricate NiTi/AZ31 composite and investigated the interfacial structure and the resulting bonding properties. A remarkable enhancement in the composite's mechanical properties was achieved, with the ultimate tensile strength (UTS) increasing by 178% upon the addition of NiTi fibers. TEM observation revealed the formation of a continuous nanocrystalline-amorphous reaction layer at the NiTi/AZ31 interface. This layer, measuring 0.1–2.0 μm in width, plays a crucial role in interfacial bonding by ensuring strong mechanical and chemical interaction between the matrix and the reinforcement. At the edge of the NiTi fibers, cubic Ti-rich Ti_2Ni precipitates were observed, accompanied by screw dislocations. These microstructural features were attributed to the non-equilibrium distribution of Ti and Ni at the interface during processing, leading to localized compositional fluctuations. The NiTi phase exhibited a distinct orientation relationship with Ti_2Ni precipitates, specifically: $[-42-1]_{NiTi}//[-112]_{Ti2Ni}$, $(132)_{NiTi}//(111)_{Ti2Ni}$. Additionally, the angular mismatch between the lattice planes of NiTi and Ti_2Ni was measured to be only 6.27° (Fig. 10a), indicating a

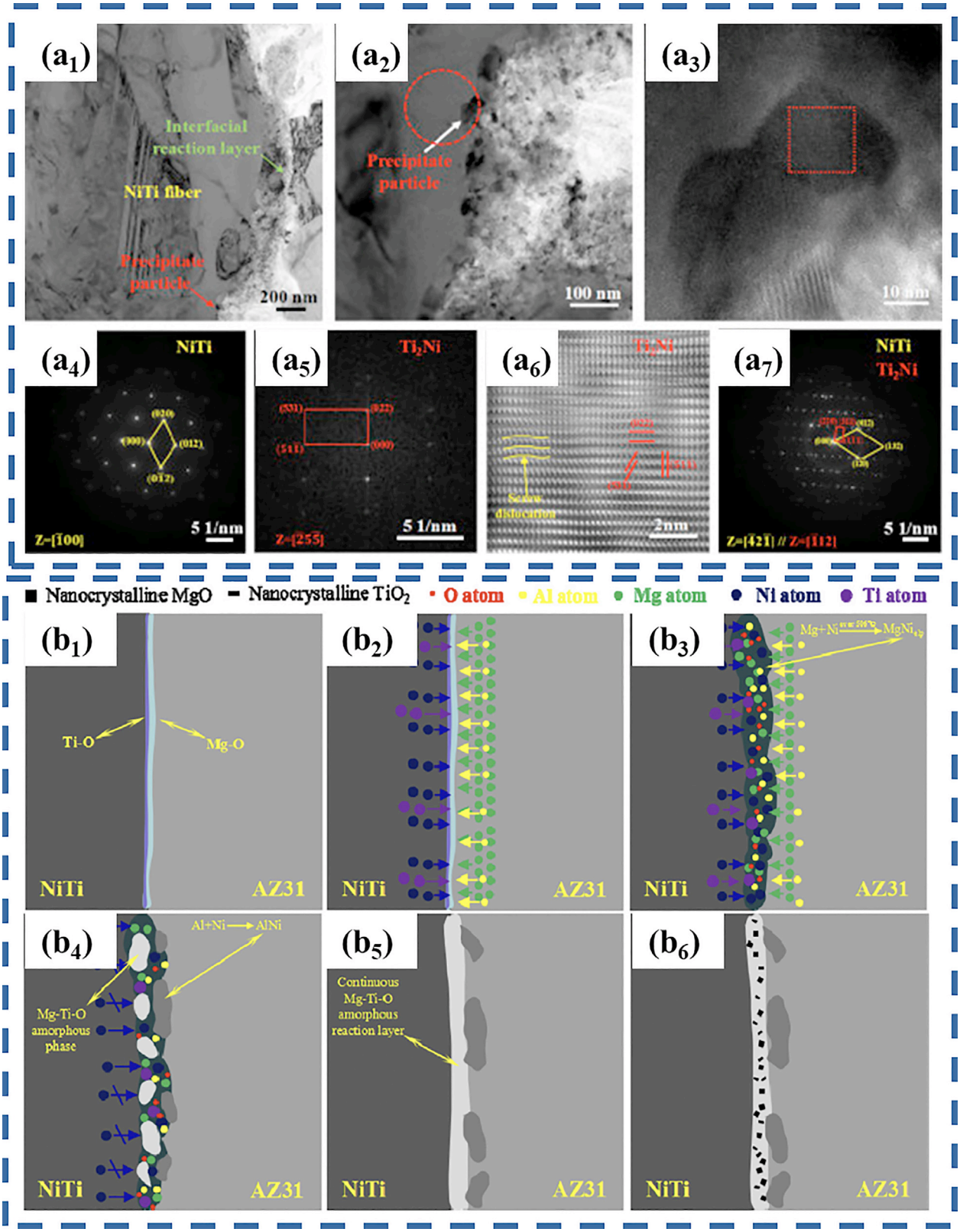

Fig. 10. TEM of NiTi fiber interface and formation mechanism. (a_{1-7}) TEM images near reaction layer; (b_1) NiTi fibers are closely connected with AZ31 matrix under pressure; (b_2–b_3) diffusion of Ni, Mg, Ti, and Al atoms leads to MgNi (with Mg, Ni, Al, Ti, and O) forming above 506 °C; (b_4) Al reacts with Ni to form AlNi; some MgNi transforms into Mg-Ti-O amorphous phase; (b_5) a continuous Mg-Ti-O amorphous layer develops at the interface with moderate O content; (b_6) excessive O results in nanocrystalline TiO_2 and MgO formation [97].

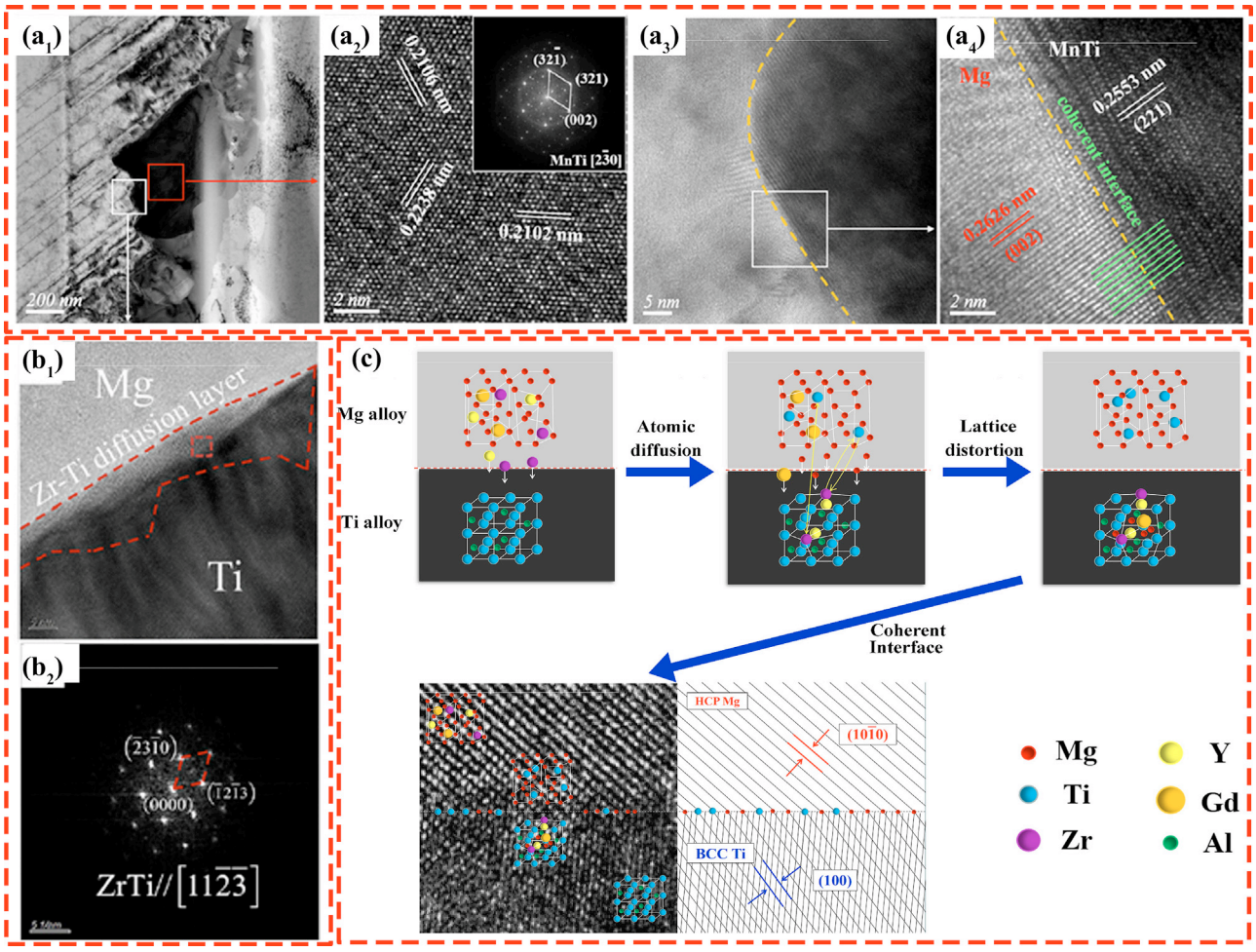

Fig. 11. Ti/Mg interface structure in Ti/Mg-RE composite: (a_1) TEM of as-homogenized Ti_P/VW94 composite; (a_2–a_4) HRTEM and FFT patterns of interface intermetallics [49]; (b_1) HRTEM of Ti/WE43 interface, (b_2) SAED pattern of highlighted region [98]; (c) Schmid image of TC4/Mg-Gd-Y-Zr interface [100].

semi-coherent interface conducive to load transfer across the phases. Furthermore, a Mg-Ni eutectic liquid phase (MgNielp) forms at the NiTif/AZ31 interface, which significantly accelerates the diffusion of Ni, promoting the growth of interfacial reaction products. Adjacent to the nanocrystalline-amorphous reaction layer on the AZ31 matrix side, AlNi particles and MgNielp were identified, as vividly depicted in Fig. 10b. These features completed the interfacial structure, contributing to both interfacial bonding strength and enhanced mechanical properties of the composite.

3.2.2. Mg-RE series matrix alloy

Mg rare-earth alloys exhibit excellent mechanical properties, which can be further enhanced by introducing Ti reinforcements. Specifically, introducing Ti reinforcements into the Mg-RE matrix results in the formation of intermetallic compounds that distinct from those in the Mg-Al-Zn matrix. For example, in Ti/Mg-RE-Mn composites, as shown in Fig. 11a, Mn diffusion at the Ti/Mg interface leads to the formation of a MnTi intermetallic transition layer. This coherent interface enables efficient load transfer and strengthens the composite. Similarly, in Ti/Mg-RE-Zr composites, Tang et al. [98] revealed the presence of a Zr-Ti diffusion layer (Fig. 11b), which acts as an intermediate layer, facilitating strong interfacial bonding between Ti particles and the Mg matrix. Furthermore, Ti reinforcements induce grain refinement in Mg-RE alloys, as observed in Ti/Mg-Y-Nd-Zr composites. Increasing Ti particle content promotes the alternate distribution of Ti particles and fine second phases within the matrix, serving as nucleation sites and resulting in a refined grain structure [99].

Moreover, the primary interfacial products in Ti/Mg-RE-Zr composites include a Zr-Ti diffusion layer and Y_2O_3 particles, with the Zr-Ti layer playing a crucial role in strengthening interfacial bonding by improving structural compatibility. Additionally, the diffusion and substitution of rare elements, e.g., Gd, Y, and Er, contribute in reducing the crystal plane mismatch between Mg and Ti. As shown in Fig. 11c, Li et al. [100] examined the interfacial diffusion of Ti, Gd, Y, and Zr. Their research revealed enrichment of Zr and Y on the Ti side of the interface. This complementary diffusion behavior stabilizes the interface by promoting atomic-level alignment and efficient bonding between Mg and Ti.

Table 3
The summary of intermetallic compounds near the interface reaction layer region in various Ti-Mg composites fabricated by different process methods.

Reinforcement	Matrix	Processing	Intermetallic compounds	Ref.
Ti	AZ91	HPS + Ext.	$Mg_{17}Al_{12}$ and Al-rich	[101]
Ti	AZ31	PM + Ext.	TiAl and MgO	[102]
Ti	AZ61	PM	Al_3Ti	[103]
Ti	AZ81	Stir cast	AlTi	[104]
Ti	WE43	HPS	Zr-Ti and Y_2O_3	[98]
Ti	VW94	Stir cast	MnTi	[49]
TC4	AZ31	Stir cast + Ext.	TiAl and Ti_3Al	[32]
TC4	AZ91	PM	Al_8Mn_5, Al_3Ti, and $Mg_{21}(Zn, Al)_{17}$	[96]
		Stir cast	Al_3Ti	[105]
TiNi	AZ31	HP	AlNi and $MgNi_{elp}$	[97]

3.2.3. Improvement of interfacial strength

The reaction between the Mg matrix and the reinforcing phase leads to the formation of interfacial compounds at the interface. The composition, structure, and properties of these interfacial compounds are critical in determining whether the interface can effectively facilitate load transfer. Table 3 provides a summary of the intermetallic compounds present in the interface reaction layer region of various Ti-Mg composites. The diversity of interfacial reaction products presents a challenge in modulating the interface, which can hinder the performance improvement of Mg-matrix composites. For achieving strong metallurgical bonding between Mg and Ti, the selection of appropriate interfacial reaction products is critical. Previous studies have shown that elements such as Al, Ni, and Cu are effective as interlayers for promoting strong bonding at the Mg/Ti interface. These interlayers facilitate the formation of intermetallic compounds and diffusion layers, which enhance interfacial bonding and load transfer across the joint.

As illustrated in Fig. 12a-b, interface microstructure and mechanical properties in Mg/Ti systems are highly sensitive to the thickness of the Cu coating. A study reported that the optimal Cu interlayer thickness for TC4/AZ91D bimetal was 36.7 μm, at which the maximum fracture strength of 65.3 MPa was achieved. This enhancement in bonding strength was attributed to the formation of Mg_2Cu and Cu_2Mg intermetallic phases, which contribute to strong interfacial adhesion through chemical stability and metallurgical compatibility [55]. Zhang et al. [106] further explored the role of Cu coatings in a Ti/AZ91 composite fabricated via a powder metallurgy (PM) method, characterizing elongated twins around the AlCuMg phase, as shown in Fig. 12c.

Apart from Cu coating, Al interlayer and Zn/Al composite interlayer have been used to fabricate TC4/AZ91D bimetal composite, aimed to achieve a high-strength Ti/Mg bimetallic composite with a metallurgical bonding interface. Zhao et al. [50] reported that the shear strength of TC4/AZ91D composite increased significantly from 48.5 MPa to 67.4 MPa with the bimetal Al/Zn coated layer, as shown in Fig. 13a. This enhancement was attributed to the transformation of interfacial compounds from $Al_{12}Mg_{17}$ + δ-Mg eutectic structure to α(Al)(Zn) + $Mg_{21}(Al, Zn)_{17}$, effectively preventing the formation of the $Al_{12}Mg_{17}$ phase. A similar phenomenon was also reported by Zhang et al. [107]. Furthermore, the effective dissolution of Zn nanoparticles into the Mg matrix reduced the solid solubility of Al element and suppressed the precipitations of submicron-sized $Mg_{17}Al_{12}$ particles, as illustrated in Fig. 13b.

3.3. Deformed structure of Mg-Ti composites

Generally, the deformation behavior of Ti-Mg composites significantly differs from that of Mg alloys, primarily due to the activation mode of dislocations. In Ti-Mg composites, a notable feature arises from the particle deformation zone, which forms in the vicinity of the reinforcing Ti particles. This region is characterized by a high density of dislocations and a large orientation gradient, caused by the deformation mismatch between the Ti particles and Mg matrix [108,109]. The particle deformation zone is critical as it allows the reinforcement to coordinate the deformation of the matrix and reduces stress concentrations by obstructing dislocation motion, thereby improving overall mechanical performance. Using digital image correlation (DIC) technology, Luo et al. [96] observed strain distribution during the tensile test of AZ91 and TC4/AZ91 (5 wt.% TC4) composites. At a strain of 7.33%, the AZ91 sample exhibited significant local strain concentration (Fig. 14a_1), whereas the TC4/AZ91 composite maintained uniform strain distribution up to a strain of 9.92%. The strain distribution maps further showed that the average strain in the TC4/AZ91 composite was more evenly distributed along the tensile direction, indicating that Ti reinforcement improves the composite's deformation uniformity and resistance to local stress concentration, as illustrated in Fig. 14a_2.

The introduction of TC4 particles effectively mitigates plastic deformation at local stress concentrations, thereby alleviating strain concentration to some extent. During deformation, TC4 particles undergo plastic deformation, directly affecting their ability to accommodate stress within the composite. Studies by Fan et al. [110] and Wang et al. [65] further investigated this phenomenon in detail. Grid nanoindentation, as shown in Fig. 14b, illustrated an increase in nanohardness within the Ti particles after the tensile test. The in-

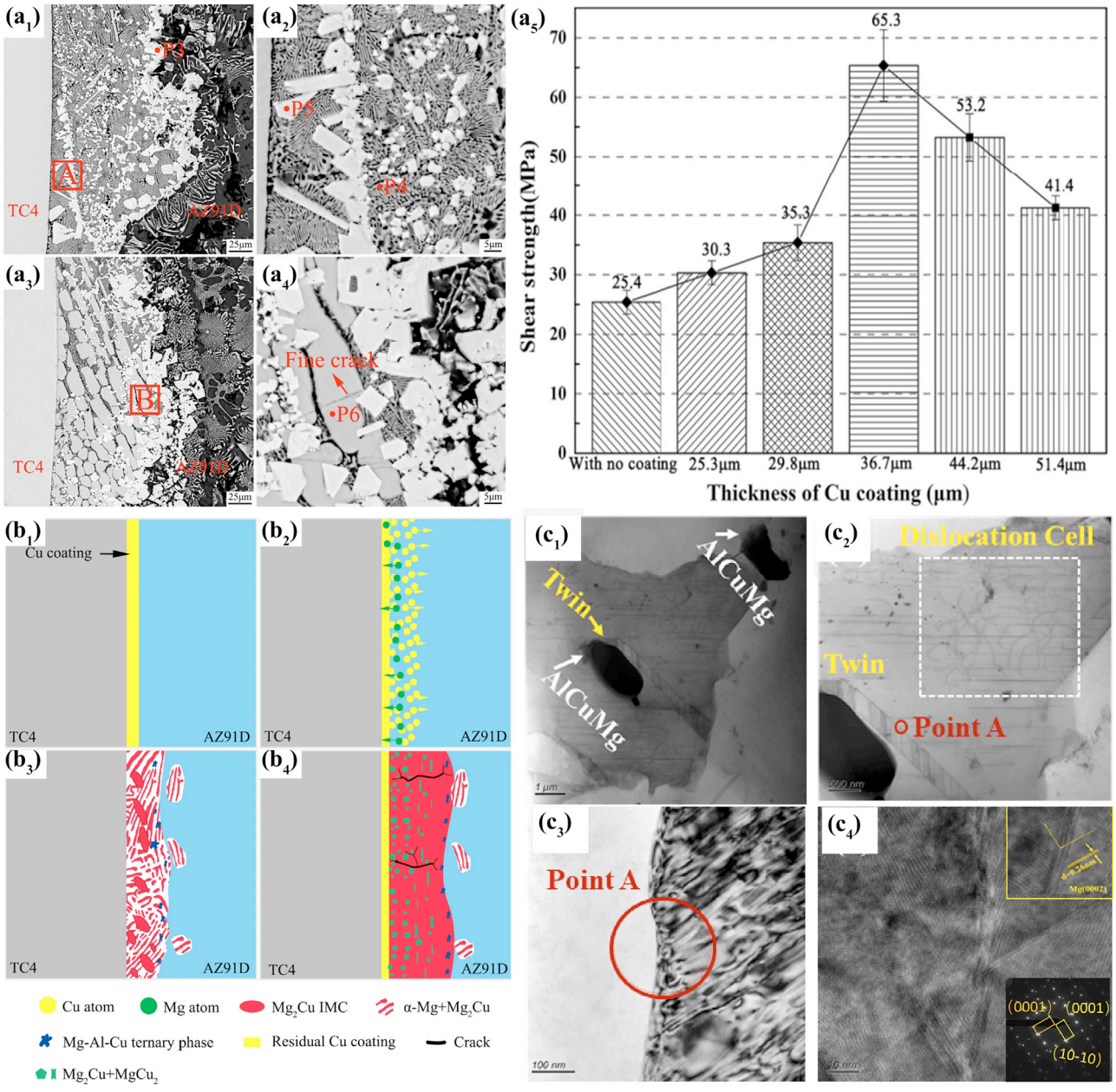

Fig. 12. Microstructure of Ti/Mg-Al-Zn bimetal interface with the Cu coating: (a_1-a_4) interface microstructure and shear strength of TC4/AZ91D bimetals with varying Cu coating thicknesses; (b_1-b_4) schematics illustrating bonding mechanisms: filling process, and Cu/Mg diffusion at the interface [55]; (c_1-c_4) TEM images of Cu-coated Ti/AZ91, showing elongated twins near the AlCuMg phase at the surface [106].

crease in hardness correlates with a rise in dislocation density inside the particles, confirming that plastic deformation occurs within the particles. These findings highlight that TC4 particles not only serve as load-bearing reinforcements but also actively participate in the deformation process by accumulating dislocations and contributing to energy dissipation. Furthermore, the EBSD technology was employed to characterize the co-deformation behavior of Ti particle within the Mg grain, as shown in Fig. 14c. The value of KAM within Ti particles increases with the deformation increment, illustrating that the deformable Ti particles are capable of undergoing co-deformation with the matrix during tensile loading. As illustrated in Fig. 14d, Ai et al. [111] reported a higher density of GNDs near Ti-Mg domain boundaries, as well as near Ti-Ti and Mg-Mg grain boundaries. This observation manifests the strain partitioning phenomenon during tensile plastic deformation of Ti-Mg MMCs, which is attributed to heterogeneous deformation induced (HDI) strengthening.

Microstructural heterogeneities in the Ti-Mg laminates were systematically studied by Chen et al. [112], as shown in Fig. 15. During plastic deformation, the mismatch between the Mg and Ti phase induces a pronounced strain gradient, resulting in the accumulation of GNDs at the interface. This, in turn, leads to enhanced HDI strengthening and work hard-

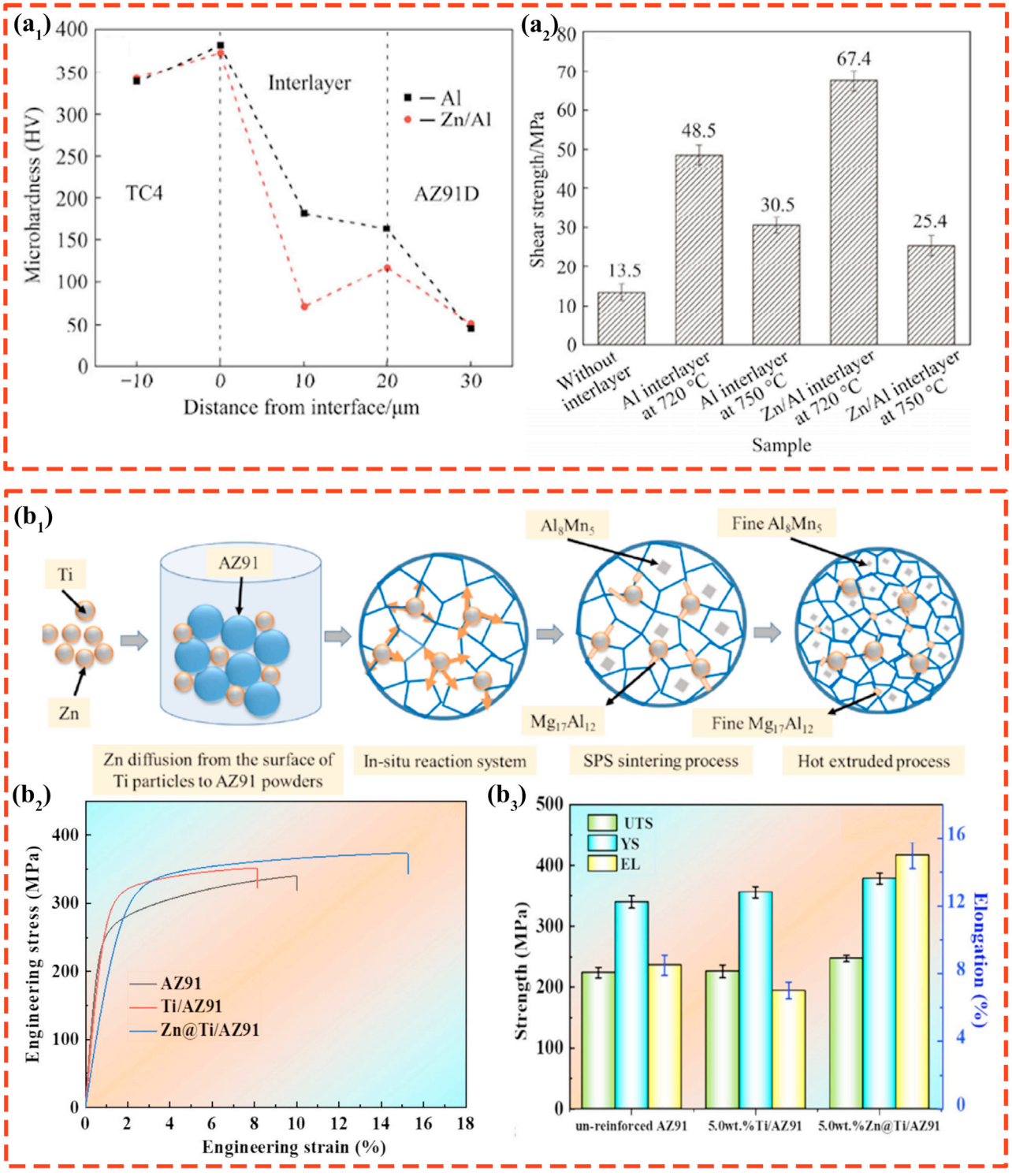

Fig. 13. Mechanical properties of Ti/Mg-Al-Zn composites with different interlayers: (a_1-a_2) TC4/AZ91D bimetal with different interlayers [50]; (b_1-b_3) schematics of submicron precipitation formation and mechanical properties for different interlayers [107].

ening compared to single-phase Mg laminates. Additionally, stress redistribution at the heterointerface promotes more uniform deformation, significantly improving ductility.

Previous investigations suggest the addition of reinforcement particles significantly alters the deformation mechanisms of the Mg matrix, including in (10–12) twinning and slip type, under certain stress states. This modification directly influences the mechanical properties of the composites. Hence, it is necessary to investigate the deformation behavior of MMCs during the deformation process. Wang et al. [113] counted the activated slip system of Mg-Al-Zn matrix and Ti/Mg-Al-Zn composites under uniaxial tensile stress using slip trace

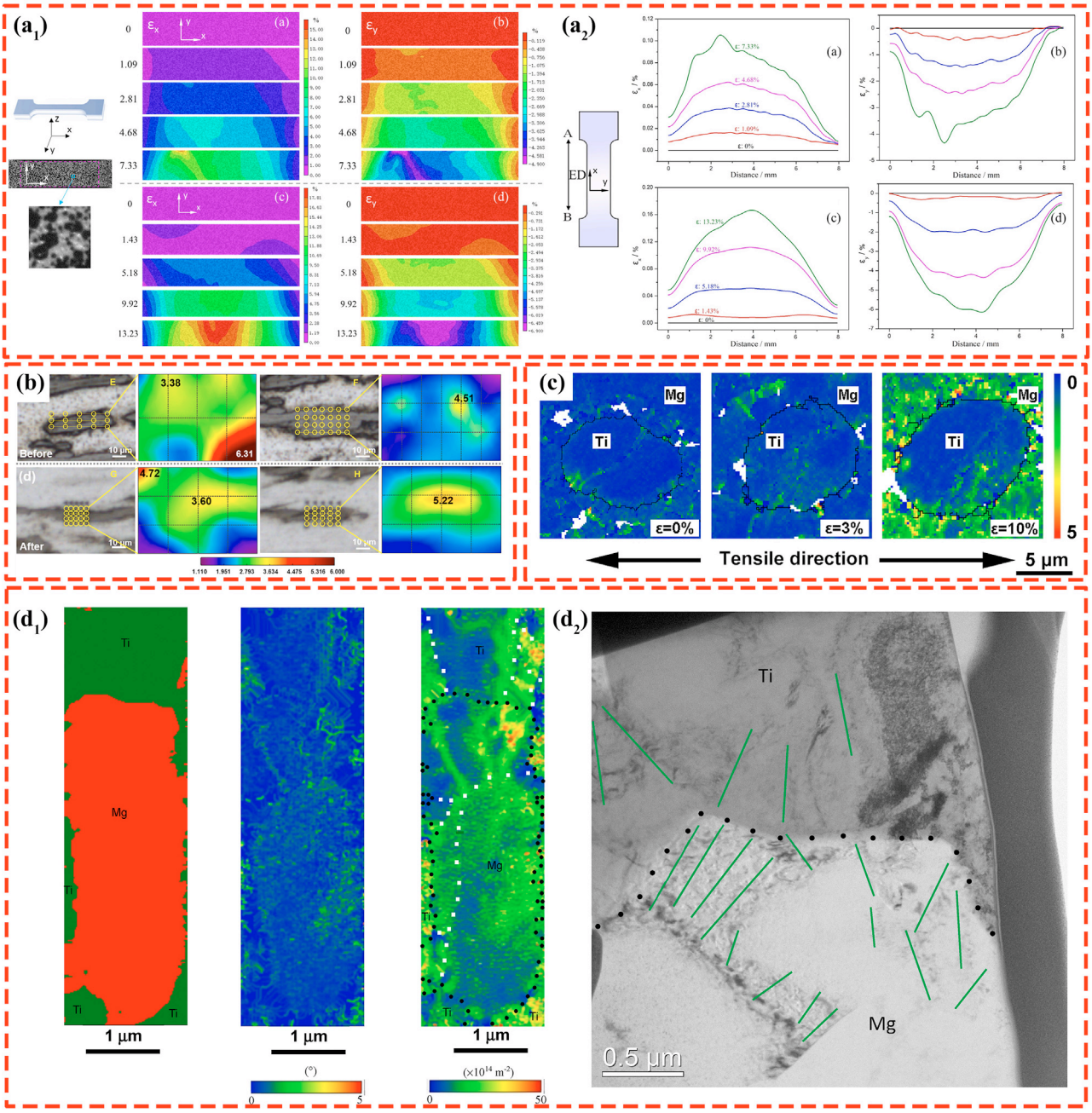

Fig. 14. Strain concentration distribution of Ti/Mg composites under room temperature tensile loading. (a_1) DIC strain maps of AZ91 and TC4/AZ91; (a_2) corresponding strain concentration curves [96]; (b) grid nanoindentation results for Ti/Mg-Zn-Ca composites before and after tension [110]; (c) KAM maps showing strain evolution in TC4/Mg-Gd-Zn composites at different strains [65]; (d_1) phase, KAM, and GND density maps of Ti-12Mg at ~5% true strain, (d_2) TEM images of GNDs, with the Ti-Mg domain boundary marked with black dots [111].

method, as shown in Table 4. The results indicate that the incorporation of Ti reinforcement suppresses the activity of basal slip, while activating a higher number of non-basal slips, particularly 2nd order pyramidal $<c + a>$, during the deformation process. The essence of the aforementioned structural deformation lies in the dislocation and twinning behaviors, which are closely related to the Schmidt factor (SF).

Sahoo et al. [23] addressed the tension-compression yield asymmetry in-situ TiB_2-reinforced Mg-based composites, and their findings were used to clearly interpret the deformation slip/twining behavior through SF calculation; that is, TiB_2 intervention increased the SF_{basal} and $SF_{tension\ twin}$. As illustrated in Fig. 16a_1-a_3, the activation stress varied at different loading angles for basal, prismatic, and twinning. The introduction of Ti particles affects the texture of the Mg matrix by tilting the angle between the *c*-axis and the uniaxial stress axis of the Mg matrix grains. This, in turn, reduces the activation stress required to initiate non-basal slip and, while

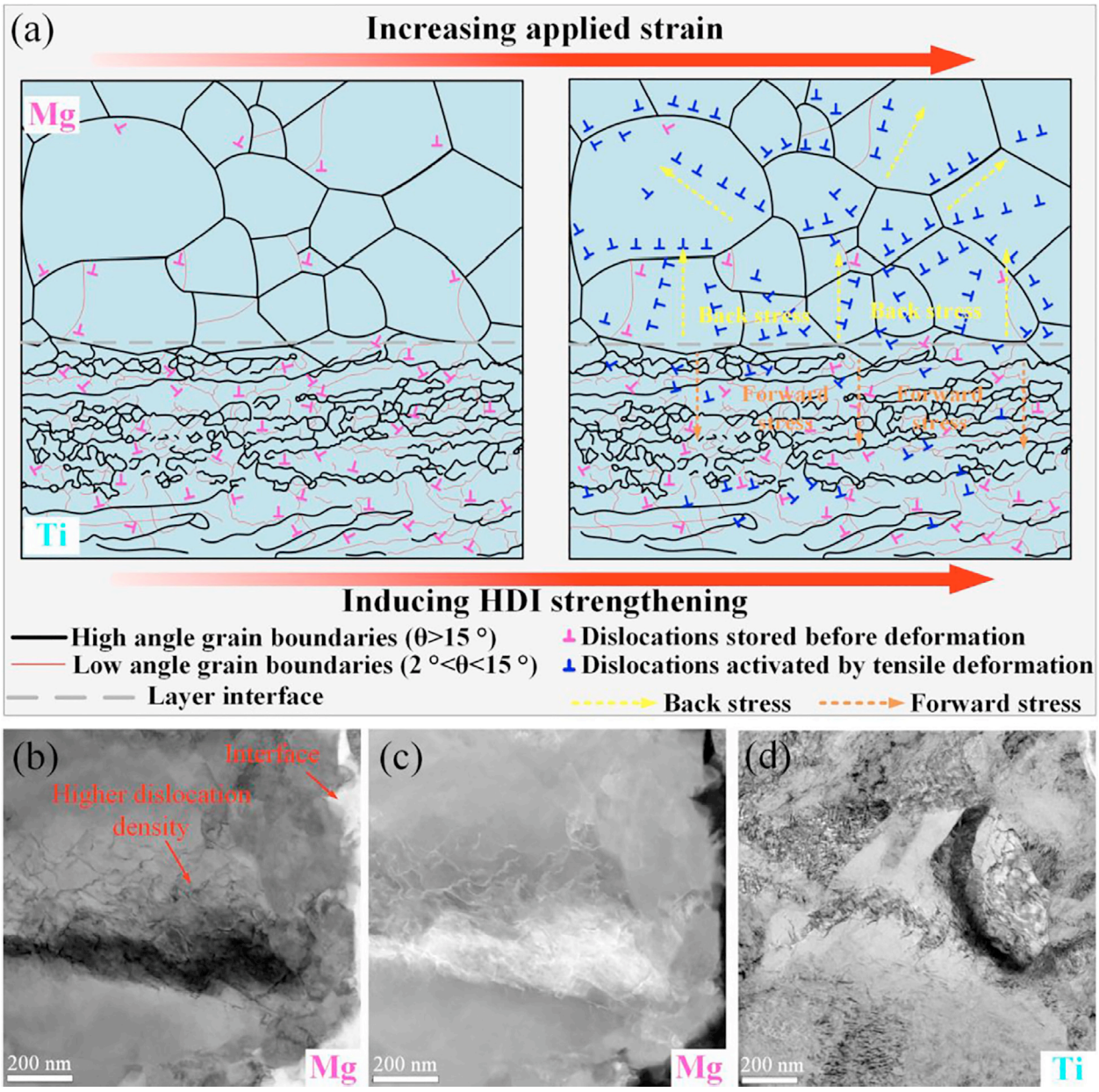

Fig. 15. Microstructure and deformation mechanisms of HDI-strengthened Ti/Mg laminated composites. (a) Schematic of microstructure evolution under tension; (b) TEM bright-field image; (c) DF image showing dense dislocations near the Mg interface after ~5% strain; (d) dislocation entanglement in Ti layer [112].

Table 4
Fractions of grain favoring basal <a> slip, prismatic <a> slip, 1st order pyramidal <a> slip, and 2nd order pyramidal <c + a> slip during tension along RD of various samples [113].

Samples	Basal <a>	Prismatic <a>	1st order pyramidal <a>	2nd order pyramidal <c + a>
AZ91	60.3%	9.5%	12.7%	17.5%
GNPs+Ti/AZ91	50.0%	10.0%	14.5%	25.5%

inhibiting the initiation of tensile twinning. Previous studies have found that, under the same uniaxial stress state, the SF value for non-basal slip in composites is slightly higher than in the matrix alloy materials, resulting in easier activation of non-basal slip [65,113–115]. As illustrated in Fig. 16b_1-b_8, the m_{basal} of GNPs + Ti/AZ91 composites decreased from 0.26 to 0.20, while the $m_{prismatic<a>}$, $m_{1st\ order\ pyramidal<a>}$ and $m_{2nd\ order\ pyramidal<c\ +\ a>}$ increased. Additionally, Pu et al. [115] utilized TEM to characterize the deformation mechanisms in Ti/Mg-Al-Zn composites after tensile deformation.

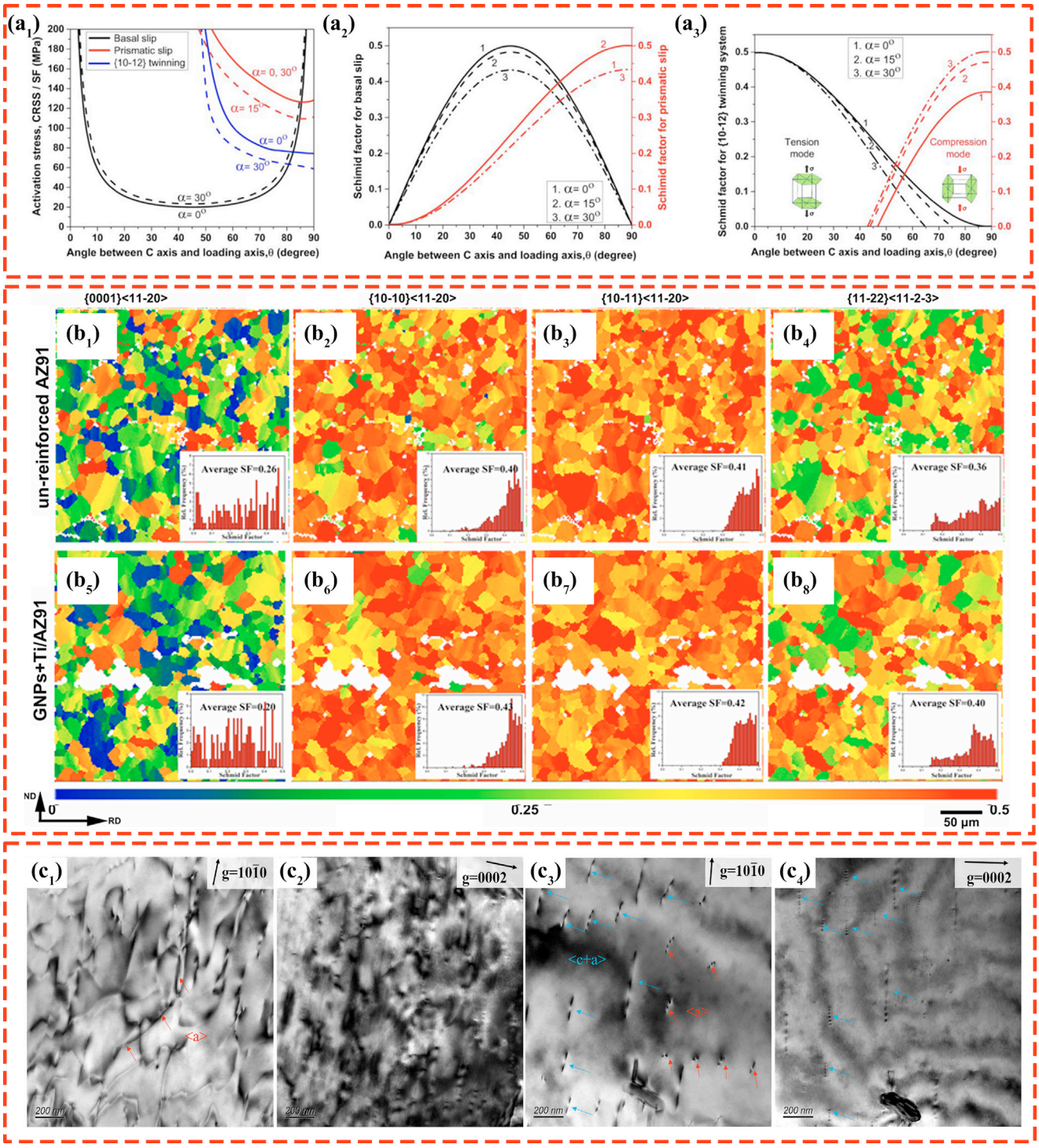

Fig. 16. Variation of deformation parameters and dislocation structures. (a_1) Activation stress, (a_2) Schmid factor of basal, prismatic slip and (a_3) Schmid factor for (10–12) twinning with angle θ [23]; (b_1–b_4) Schmid factors of various slip systems in unreinforced AZ91, and (b_5–b_8) GNPs + Ti/AZ91 composites under RD tension [113]; (c_1–c_2) dislocation structures in AZ91 alloy, and (c_3–c_4) in Ti_P/AZ91 composite after tensile deformation [115].

By applying the dislocation visibility principle ($\boldsymbol{g}^*\boldsymbol{b} = 0$), they identified the dislocation components, revealing that the density of <*c*> type dislocation in composite was significantly higher than in the matrix alloys, further confirming the substantial role of Ti particles in enhancing the non-basal slip activity of Mg matrix.

Micron-sized Ti reinforcements have a limited effect on grain migration and rotation; however, studies by Wang et al. [116,117] have shown that Ti reinforcements still contribute to a noticeable weakening of basal texture. As vividly illustrated in Fig. 17, each micron-sized Ti particle generates a stress field that affects the material in the vicinity of the in-

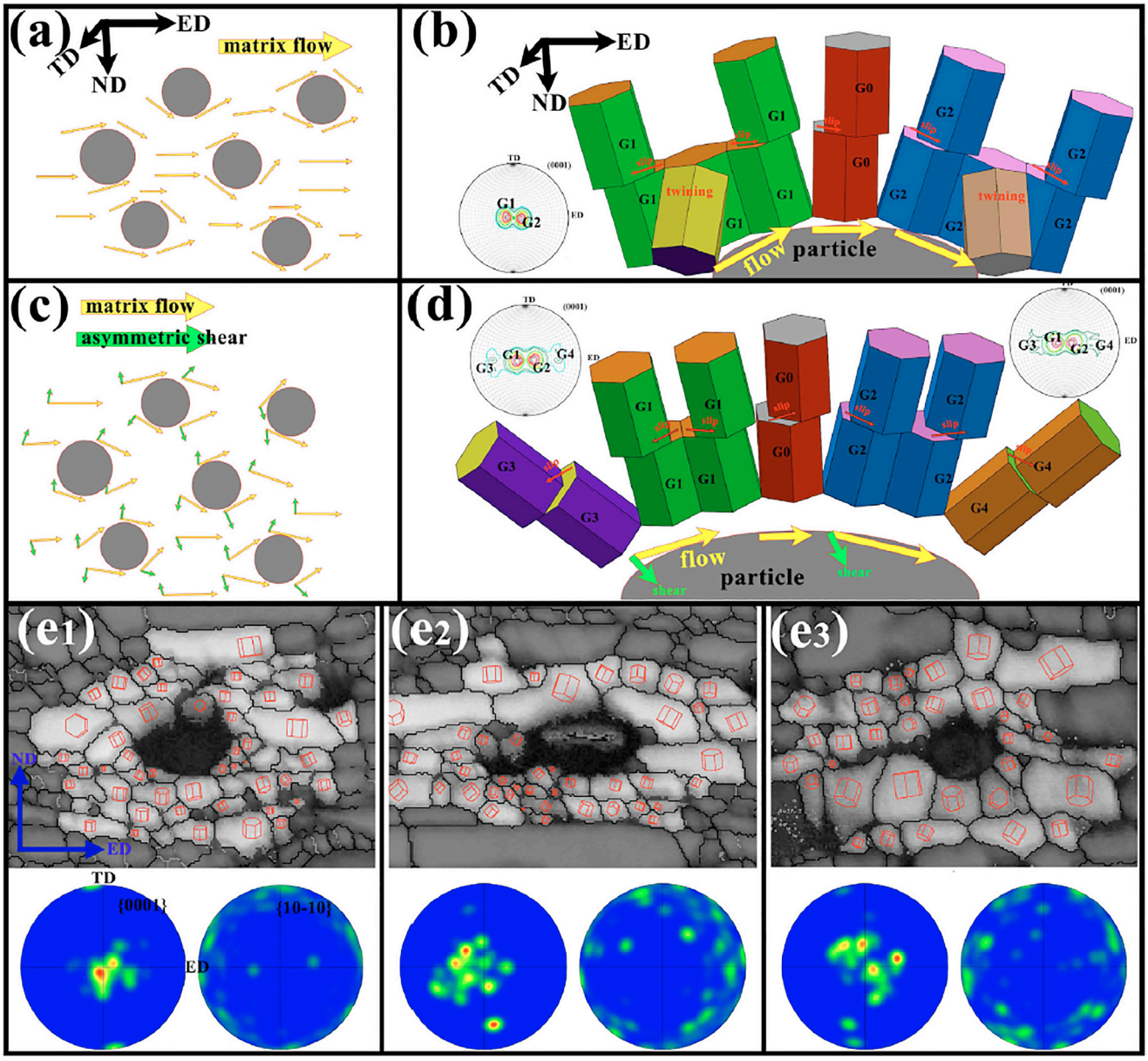

Fig. 17. Schematic diagram of flow behavior, texture evolution, misorientation, and twining behavior during extrusion [116].

terface. This stress field alters the defluxion amplitude of the *c*-axis, thus weakening basal texture. It can be anticipated that such a particle-induced stress field will be present in micron-reinforced MMCs even during sample uniaxial tension. In this context, the classical uniaxial loading SF model may not fully capture the effects of the complex stress state. Several studies have investigated the changes in SF under complex stress state, and have proposed the three-dimensional (3D) SF models [118–120]. These models assume that a crystal is subjected to a stress tensor, making them more applicable for computing the SF values in the presence of particle-induced stress field. However, research in this area remains limited, and further exploration is needed to understand and profile the SF behavior in MMCs.

4. Micromechanical constitutive model

Micromechanical constitutive models reveal the deformation mechanism and performance of materials under different loading conditions [121–124]. These models establish a quantitative connection between a material's microstructure and its response. Such models not only provide a theoretical basis for an in-depth understanding of the mechanical behavior of materials but also serves as a critical tool for optimizing design, processing, and performance. For example, Yu et al. [125] presented the typical microstructural characteristics of Mg-20% NiTi composites based on optical microscope diagrams (as shown in Fig. 18a) and established a micromechanical constitutive model for Mg-NiTi composites

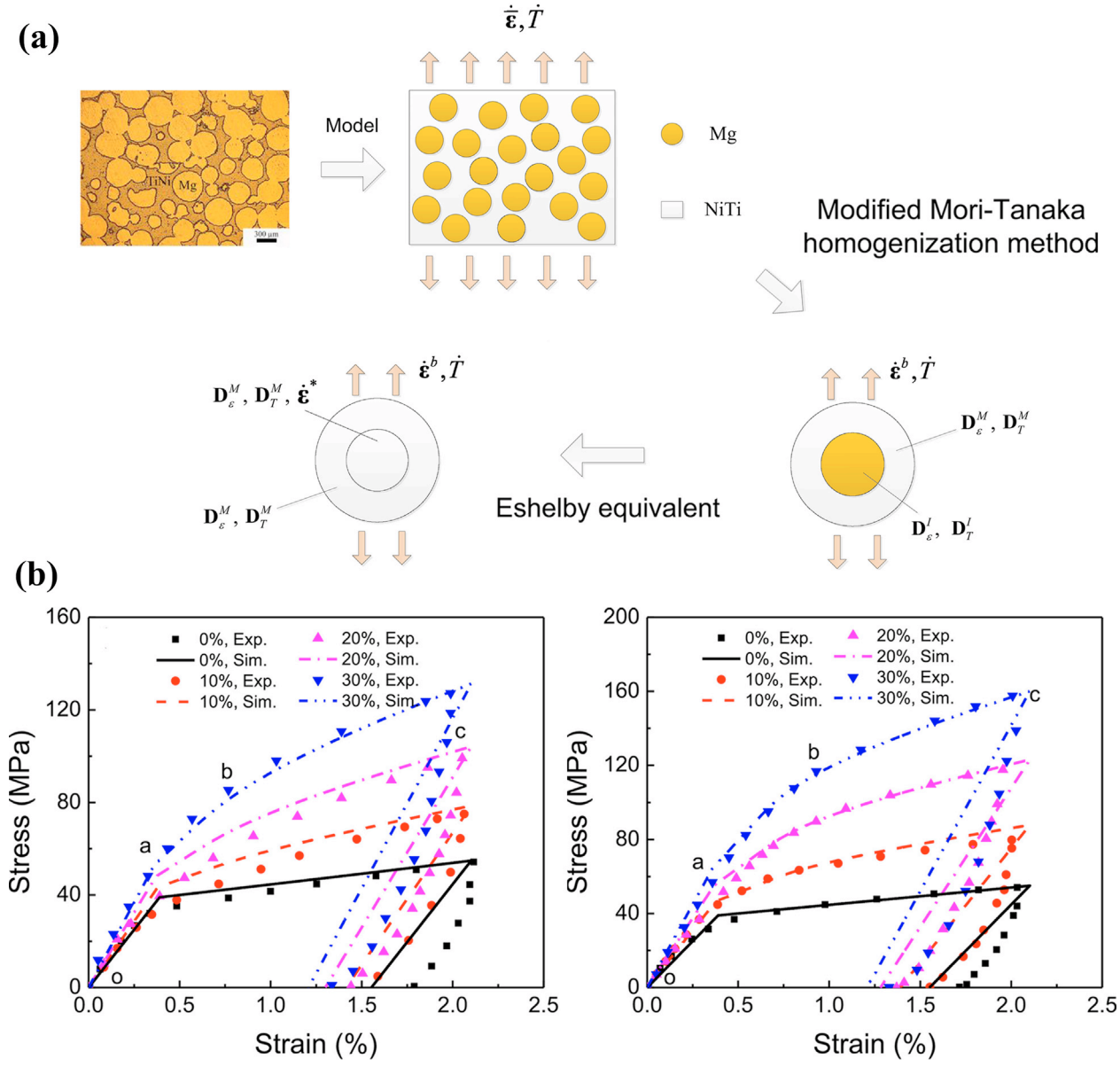

Fig. 18. Micromechanical model for temperature-dependent deformation in Mg–NiTi composites. (a) Microstructure and modeling schematic, (b) experimental and predicted stress-strain curves at different temperatures of Mg-NiTi [125].

to describe their abnormal temperature-dependent deformation (as depicted in Fig. 18b). The authors applied a modified Mori-Tanaka homogenization approach, which is based on Eshelby's tensors for spherical inclusions embedded in a spherical domain, to model the interactions between the phases and predict the stress-strain response of the composite. For NiTi shape memory alloys, an elastic-plasticity ontological model incorporating a nonlinear plastic hardening law was chosen to more accurately predict the stress-strain relationship of Mg-matrix composites under complex loading conditions. In addition, Luo et al. [101] investigated the impact of varying Ti particle sizes on the nonlinear elastic behavior of Ti-reinforced MMCs, and the stress-strain nonlinear mechanical principal model elasticity relationship of composites was corrected, i.e., the equation is: $\sigma = \varepsilon/(1/E + \varepsilon/\sigma_p)$. This model enabled the simulation of the mechanical properties of composites reinforced with Ti particles of varying sizes (5, 15, 38, 45 μm), providing valuable insights into how particle size influences the overall mechanical response.

To promote the industrial application of Mg matrix composites, the strain-compensated Arrhenius constitutive model was utilized to accurately predict the hot deformation behavior [126–129]; moreover, the processing map was used to optimize hot processing technology, thereby preventing the occurrence of defects [130]. For Ti-reinforced Mg composites, Chen et al. [131] developed an Arrhenius principle model and assessed its correctness using error anal-

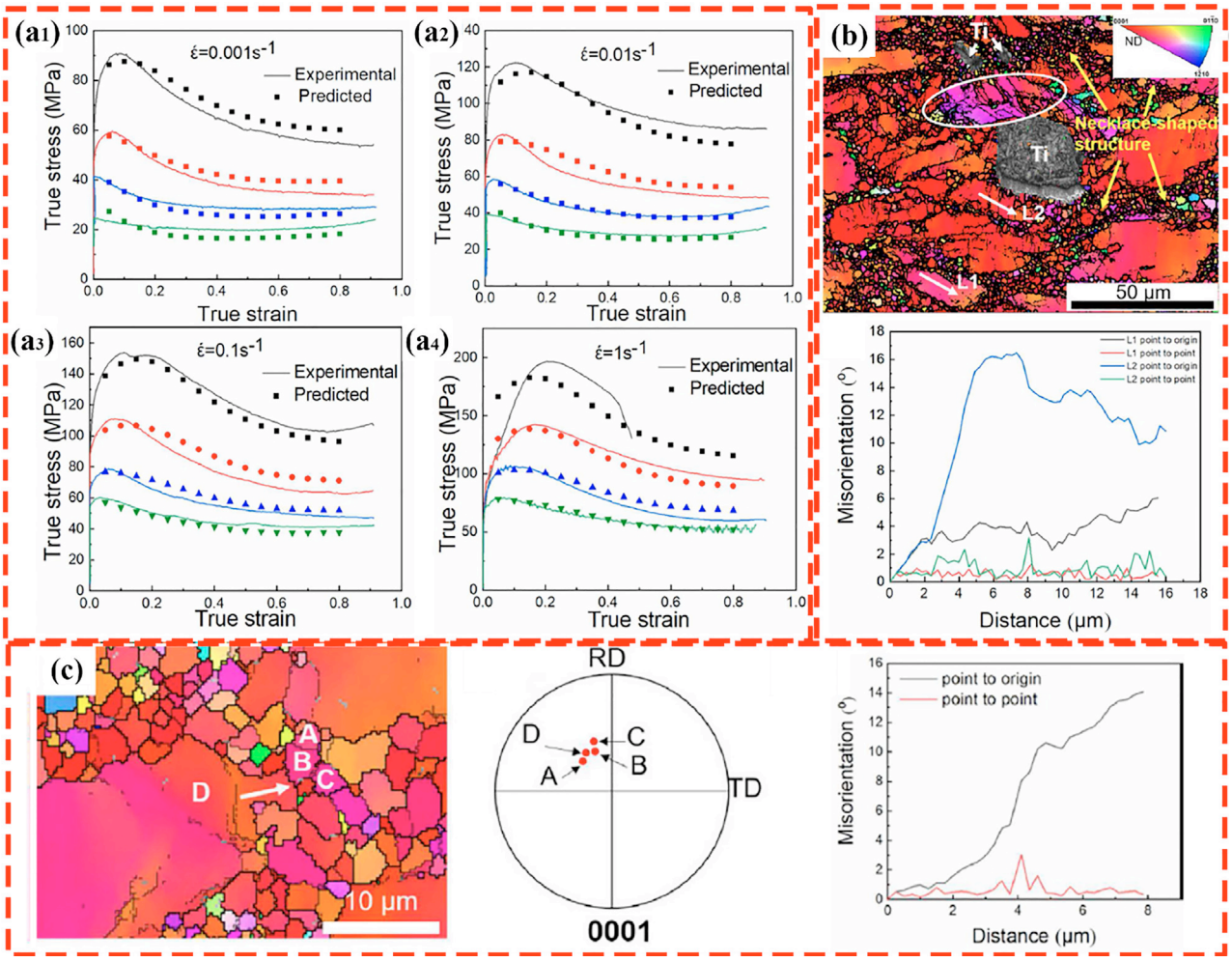

Fig. 19. The flow stress-strain behavior and evolution microstructure of Ti/AZ91 composite. (a) Predicted vs. experimental flow stresses; (b) Mg grain tilting induced by Ti particles; (c) nucleation and growth of DRX grains around deformed grains [131].

ysis. The strain-compensated Arrhenius model and Zener-Hollomon parameters were obtained by fitting the equation with a fifth-order polynomial and adding material constants. The simulation results based on this correction formula are shown in Fig. 19a. In addition, the particle-stimulated nucleation (PSN) phenomenon was observed around Ti particles, as depicted in Fig. 19b-c, which is attributed to decreasing the calculated activation energy. However, the thermal deformation constitutive modeling of other systems of Mg matrix, e.g., Mg-RE, Mg-Zn-Ca, Mg-Al-Mn, has been less studied, and the effect of Ti particles on other series of Mg matrix is still unclear, which need further exploration.

Accurate constitutive modeling in metal matrix composites demands a synergy of theoretical, computational, and experimental methods to address their microstructural complexity and multi-scale effects. Experimental approaches are indispensable for quantitative insights, enabling the development of reliable models for optimizing composite performance.

5. Mechanical and physical properties

5.1. Mechanical properties

5.1.1. Room temperature tensile properties

The tensile and compression properties of Mg-Ti composites are significantly influenced by the interfacial bonding between Ti particles and the Mg matrix. As the volume fraction of Ti particles increases, a greater amount of loading stress can be transferred to the particles, which leads to an increase in both the yield and tensile strength of the MMCs. However, when the volume fraction of Ti reaches a critical threshold, interfacial reaction with Mg matrix results in the formation of compounds at the interface. This weakens the interfacial bonding strength and, in turn, reduces the tensile strength and plasticity of the Mg-Ti composite. As mentioned in Section 2, various preparation methods for Ti particle-reinforced Mg-based composites were reviewed. These different methods result in variations in the content, size, distribution, and morphology of Ti particles within the Mg matrix, which, in

turn, influence the composite's mechanical properties, as further detailed in Section 3. A systematic comparison of the yield strength, ultimate tensile strength, and elongation at room temperature for Mg-based composites with varying Ti particle content is provided in Table 5.

When Mg is used as the matrix, Mg-Ti composite, prepared by PM combined with the hot extension method, has superior mechanical properties compared to DMD combined with hot extension preparation process. Sankaranarayanan [132] et al. mixed micron-Ti and nano-Cu ball-milled (5.6 wt.%Tip+3 wt.%Cu), using PM combined Hot extension, Nano-Cu addition formed Mg_2Cu intermetallics, enhancing strength while maintaining ductility. The Ti_3Cu phase formation and strong matrix interfacial bonding through pre-processing further improved the composite's mechanical properties.

Compared with PM combined with hot pressing, the mobility of the better AZ series alloy as a matrix in composites is more used in the stir casting combined with the hot extension preparation process. During hot extrusion, TC4 particles induce particle deformation zones, promoting matrix dynamic recrystallization nucleation and grain refinement. The best overall mechanical properties were obtained by adding 10 vol.%TC4 particles, with yield strength, tensile strength, and elongation of 249 MPa, 369 MPa, and 6.4%.

The Tip/Mg-6Zn-0.2Ca composite extruded at 240 °C and 0.1 mm/s exhibited high strength (YS: 383.6 MPa, UTS: 404.8 MPa) and decent elongation (4.8%). This enhanced performance stems from fine grain structure, refined $MgZn_2$ phases, and elongated Ti particles. Initially, the Tip/Mg-6Zn-0.2Ca composite shows a higher work hardening rate than the Mg-6Zn-0.2Ca alloy due to Ti particles, grain boundaries, and nanoprecipitates impeding dislocation movement [110,133]. Notably, Tang et al. [60] reported the content of Ti particle of 0–9 wt.%Ti, the 6Ti/WE43 composite exhibited an excellent strength-ductility combination, with YS, UTS, and EL of 267 MPa, 337 MPa, and 15.1%, respectively. Wang et al. [134] investigated NiTi particle reinforced the low RE-content (<6%) matrix of WE43 composites fabricated by friction stir processing (FSP). They reported that the low processing temperature during FSP effectively prevented interfacial reactions between NiTi particles and the Mg matrix. However, the addition of NiTi particles actually led to a decrease in mechanical properties. Compared to the WE43 Mg matrix, the NiTip/WE43 composite exhibited reductions in yield strength, ultimate tensile strength, and elongation by 33%, 12%, and 18%, respectively. Furthermore, an inverse relationship between NiTi particle size and NiTip/WE43 composite mechanical properties is revealed, with larger particles corresponding to diminished mechanical performance. In the high RE-content (>6%) matrix of VW94, the Ti particles reinforced VW94 composites fabricated by stir cast, which promoted the formation of RE-rich phases and led to the diffusion of Mn atoms to the edge of Ti particles, resulting in a submicron MnTi layer at the Mg/Ti interface [49], UTS and elongation of Tip (2.5 wt.%, 1–7 μm) + Tip (1.0 wt.%, 10–55 μm) /VW94 composite are 162 MPa, 240 MPa, and 7.7%, respectively. Furthermore, the semi-solid stir casting method was utilized to incorporate Ti particles into the Mg-7Gd-2Y-3Zn alloy, creating Tip/GWZ723 composites. These composites underwent extrusion at temperatures ranging from 380 °C to 450 °C, during which the aspect ratio of the Ti particles was modified based on the extrusion temperature. After hot extrusion, the Ti particles elongated along the extrusion direction, with their aspect ratio increasing as the temperature decreased, reaching 12:1 at 380 °C. This increase in aspect ratio improved the yield strength and ultimate tensile strength of the composites to 454.3 MPa and 492.2 MPa, respectively, while refining the Mg matrix and enhancing strain distribution, which helped suppress crack initiation and delay fracture [135]. The strengthening effects mainly include fine grain strengthening and load transfer strengthening [136,137]. On the one hand, the refined grain structure resulting from the extrusion process contributed to greater grain boundary area, further impeding dislocation motion and enhancing strength according to the Hall-Petch relationship. On the other hand, the elongated Ti particles facilitated a more uniform stress distribution under external loading, thereby enhancing the composite's plastic deformation capacity. Evaluating the ability of Ti reinforcement to coordinate deformation and facilitate HDI hardening during deformation is pivotal for guiding composite design, thereby overcoming the challenge of achieving synergistic strength and plasticity enhancement in MMCs. The strong interfacial bonding between the elongated Ti particles and Mg matrix enabled efficient load transfer from the softer matrix to the stiffer reinforcement, significantly increasing the overall load-bearing capacity of the composite.

Fig. 20 compares the UTS and elongation of various Mg alloys and their MMCs, focusing on the impact of reinforcement strategies on mechanical properties. Distinct symbols and color-coded regions delineate different alloys and their composites, as indicated in the legend. The value of RE-contained MMCs is significantly higher than those for conventional monolithic Mg alloys and their unreinforced counterparts, which typically cluster at lower strength and moderate ductility values. The incorporation of Ti particles into magnesium-based composites is highly effective for simultaneously improving strength and plasticity, advancing the potential of Mg MMCs for demanding structural applications requiring both high performance and mechanical reliability.

5.1.2. Elevated temperature tensile properties

Table 6 presents a comprehensive summary of the mechanical properties of Mg-Ti composites under tension testing at elevated temperatures, corresponding to various fabrication methods. Pérez et al. [149] investigated the mechanical behavior of a 10 vol.%Ti/Mg composite within the temperature range of 25 °C to 300 °C, finding that the reinforcing efficiency of Ti diminishes as temperature rises. Composites of TiNi SMA fibers with AZ31 Mg alloy plate were successfully prepared using the pulsed current hot pressing technique. A good bonding of TiNi fibers with the Mg plate was achieved at a temperature of 773 K with a total processing time of 0.6 ks. The yield strength and elongation of the composites in-

Table 5
Summary of the mechanical properties under tension testing at room temperature of Mg-Ti composites corresponding various fabrication methods.

Matrix	Reinforcement	Method	Technological parameter	Mechanical properties			Ref.
				YS (MPa)	UTS (MPs)	EL (%)	
Mg	-	DMD	Slurry: stirred at 460 rpm for 8 min;	100±4	258±16	7.7±1.2	[33,138,139]
	0.58 vol.%Tip		Ar gas flow rate: 25 L/min;	134±7	190±7	6.3±0.6	
	0.97 vol.%Tip	Hot extrusion	Hot extrusion: 350 °C/ 20.25:1;	135±3	197±8	8.3±0.6	
	1.98 vol.%Tip			162±5	231±12	7.7±0.1	
	2.2 vol.%Tip			163±12	248±9	11.1±1.2	
	4 vol.%Tip			154±10	239±5	9.5±0.3	
	5.6 vol.%Tip			158±6	226±6	8.0±1.5	
Mg	-	DMD	Slurry: stirred at 450 rpm for 5 min;	84±6	148±6	13.0±0.9	[140]
	0.5 wt.%NiTip		Ar gas flow rate: 25 L/min;	106±12	167±14	9.0±0.8	
	1 wt.%NiTip	Hot extrusion	Hot extrusion: 350 °C/ 20.25:1;	123±2	176±9	9.0±4.2	
	1.5 wt.%NiTip			163±9	187±8	9.0±0.4	
	3 wt.%NiTip			193±17	217±16	11.0±0.2	
Mg	-	PM	Milling time: 3 h;	182(+7,-4)	223(+8,-10)	14.3(+1.1,-1.3)	[141]
	1 mass.%Tip		Spark plasma sintering: 30 MPa; 600 °C/30min;	180(+6,-4)	221(+7,-9)	16.1(+1.5,-1.2)	
	3 mass.%Tip			184(+5,-8)	224(+9,-4)	14.9(+1.1,-1.0)	
	5 mass.%Tip			179(+6,-3)	218(+6,-6)	15.5(+1.4,-2.0)	
	-	PM	Milling time: 3 h;	155	221	9.4	
	3 mass.%Tip		Spark plasma sintering: 30 MPa; 600 °C/30min;	192	251	8.9	
		Hot extrusion	Hot extrusion: 400 °C/37.7:1;				
Mg	-	PM	Milling: 200 rpm; 1 h;	136±8	170±7	6.1±1.0	[132]
	5.6 wt.%Tip		Uniaxially cold compacted: 160 MPa;	151±4	190±4	4.2±0.3	
	5.6 wt.%Tip-3wt.%Cu	Hot extrusion	Hot extrusion: 350 °C/20.25:1;	197±4	225±2	2.6±0.3	
	(5.6 wt.%Tip+3 wt.%Cu)BM			223±4	253±4	4.2±0.6	
Mg	-	PM	Milling time: 1 h;	131±5	163±4	3.2±2.5	[142]
	10 mass.%Tip		Uniaxially cold compacted: 600 MPa; Sintered: 630 °C; 2 h;	141±4	212.0±5.1	11±3	
		Hot extrusion	Hot extrusion: 350 °C/5:1;				
AZ31	-	FSP	Rotational speed: 950 rpm; Traverse speed: 30 mm/min; Passes: 5; Shoulder diameter: 24 mm; Shoulder concavity: 0.2 mm; Pin diameter: 7–5 mm; Pin length: 5.7 mm; Pin shape: Frustrum of a cone; Tool material: H13 steel; Groove width: 0, 0.4, 0.8 and 1.2 mm; Groove depth: 5 mm;	98	226	14.5	[79,143–145]
	7 vol.%Tip			164	243	12.7	
	14 vol.%Tip			183	263	10.9	
	21 vol.%Tip			193	283	9.4	
	7 vol.%TC4p			170	258	12.1	
	14 vol.%TC4p			195	284	11.2	
	21 vol.%TC4p			205	322	9.3	
AZ31	-	Stir cast	Stirring: 630 °C, 5 min;	227	285	16.5	[146]
	3 wt.%Tip		Ultrasonic treatment: 1600 W, 10 min;	238	298	18.4	
	6 wt.%Tip	Hot extrusion	Hot extrusion: 350 °C/16:1;	245	327	20.4	
	9 wt.%Tip			251	316	13.6	
AZ31	-	PM	Milling: 80 rpm, 2 h;	187	272	-	[95]
	3 wt.%Tip		Hot press sinter: 500 °C, 30 min;	193	277	-	
	6 wt.%Tip	Hot extrusion	Hot extrusion: 350 °C/25:1;	199	290	-	
	9 wt.%Tip			206	274	-	

(continued on next page)

Table 5 (*continued*)

Matrix	Reinforcement	Method	Technological parameter	Mechanical properties			Ref.
				YS (MPa)	UTS (MPs)	EL (%)	
AZ31	-	PM	Milling: 80 rpm, 1 h;	237.0±2.2	271.0±3.1	4.4±0.4	[102]
	3 wt.%Tip		Cold compress: 600 MPa;	244.0±1.9	287.0±2.8	6.1±0.2	
	6 wt.%Tip		Vacuum sintered: 630 °C/2.5 h;	255.0±2.7	304.0±3.7	6.9±0.3	
	9 wt.%Tip	Hot extrusion	Hot extrusion: 350 °C/25:1;	264.0±1.9	294.0±3.4	8.0±0.6	
AZ91	-	Stir cast	Stirring: 575 °C, 900 rpm, 20 min;	-	81±6	0.7	[147]
	50 vol.%TC4p		Ultrasonic treatment: 20 kHz, 500 W, 20 min; Settling: 710 °C, 20 min;	-	154±2	0.5	
			Stirring: 575 °C, 900 rpm, 20 min;	-	116±7	0.25	
			Ultrasonic treatment: 20 kHz, 500 W, 20 min; Settling: 710 °C, 20 min;	-	160±5	0.28	
AZ91	TC4	Stir cast	Semi-solid Stir: 575 °C, 1000 rpm, 5 min; Heating and liquid stir: 700 °C, 300 rpm(heating), 250 rpm(liquid), 5 min; Solidified: under a 100 MPa pressure;	80	176	5.0	[105]
			Semi-solid Stir: 575 °C, 1000 rpm, 10 min;	120	221	3.5	
			Semi-solid Stir: 575 °C, 1000 rpm, 15 min;	130	227	2.4	
			Heating and liquid stir: 700 °C, 600 rpm(heating), 250 rpm(liquid), 5 min;	137	250	2.6	
AZ91	-	PM	Milling: 80 rpm, 2.5 h; Hot compress: 15 MPa, 500 °C, 30 min;	175	282	13.1	[96]
		Hot extruded	Hot extrusion: 300 °C/25:1;				
	5 wt.%TC4p			211	303	18.7	
	10 wt.%TC4p			208	298	14.3	
	15 wt.%TC4p			205	279	9.9	
AZ91	10 vol.%TC4p	Stir cast	Stirring: 575 °C, 250 rpm; Solidified: under a 100 MPa pressure;	125	245	3.9	[148]
	10 vol.%TC4p	Stir cast	Stirring: 575 °C, 250 rpm; Solidified: under a 100 MPa pressure;	249	369	6.4	
		Hot extrusion	Hot extrusion: 350 °C/14:1;				
Mg-Zn-Ca	Tip	Stir cast	Stirring: 615 °C for 20 min;	438	450	1.0	[110]
		Hot extrusion	Hot extrusion: 200 °C/16:1;				
			Hot extrusion: 240 °C/16:1;	383	404	4.8	
			Hot extrusion: 280 °C/16:1;	324	341	7.5	
WE43	-	PM	Ball milling: 80 r/min for 150 min; Hot-pressing sintering: 500 °C; 15 MPa for 15 min;	217.0 ± 3.1	277.0±2.5	16.2±0.6	[98]
		Hot extrusion	Hot extrusion: 500 °C;				
	3 wt.%Tip			246.0± 1.7	310.0±2.7	16.5±0.4	
	6 wt.%Tip			267.0± 2.1	337.0±1.9	15.1±0.3	
	9 wt.%Tip			281.0± 1.5	354.0±2.3	8.2±0.2	
WE43	-	FSP	Rotational speed: 600 rpm; Traverse speed: 100 mm/min; Passes: 4; Shoulder diameter: 18 mm; Shoulder concavity: 0.2 mm; Pin diameter: 6 mm; Pin length: 4.8 mm; Pin shape: Frustrum of a cone; Tool material: W18Cr4V;	119	318	18.5	[134]
	2–50 μm NiTip			79	281	15.2	
	100–150 μm NiTip			68	165	11.1	
VW94	-	Stir cast	Stir: 625 °C, 600 rpm for 5 min; 690 °C, 300 rpm for 30 s; Ultrasonic treatment: 20 kHz, 1600 W, 10 min; Stir: 300 rpm for 30 s;	145	198	5.2	[49]

(*continued on next page*)

Table 5 (*continued*)

Matrix	Reinforcement	Method	Technological parameter	Mechanical properties			Ref.
				YS (MPa)	UTS (MPs)	EL (%)	
	3.5 wt.%1-7 μmTip			145	209	6.1	
	2.5 wt.%1-7 μmTip+1.0 wt.%10-55 μmTip			162	240	7.7	
	1.5 wt.%1-7 μmTip+2.0 wt.%10-55 μmTip			155	227	6.9	
	-	Stir cast	Stir: 640 °C, 30 min;	107	134	1.0	[135]
GWZ723							
	Tip	Hot extrusion	Extrusion: 380 °C/16:1.	454	492	2.3	

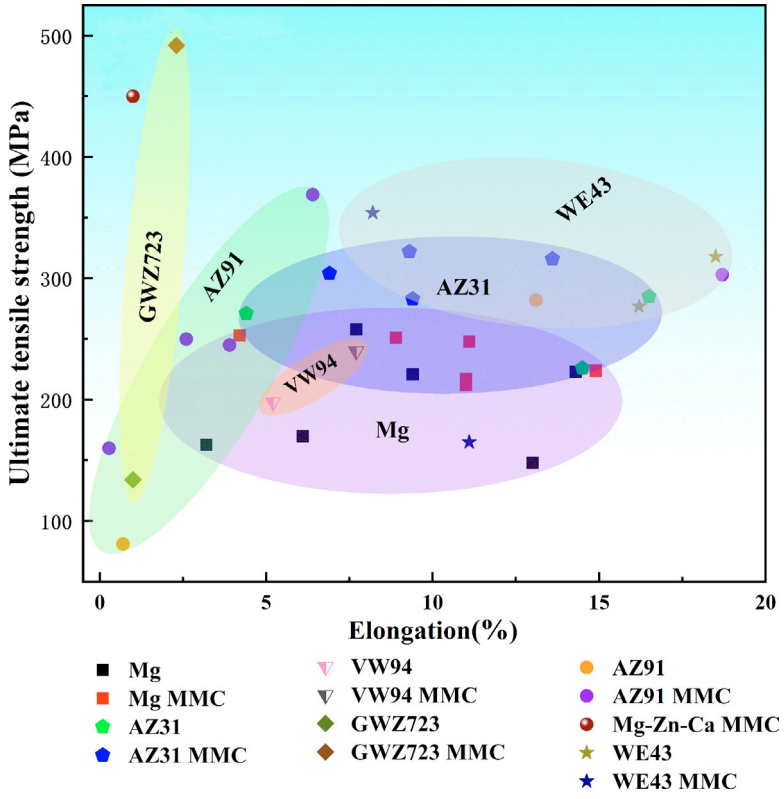

Fig. 20. Distribution maps of UTS and elongation of related Ti-reinforced MMCs at room temperature (data from Table 4).

creased with increasing temperature in the temperature range from 293 K to 423 K. In particular, the yield strengths of the composites were about 68 MPa and 87 MPa higher at 373 K and 423 K, respectively, than that at 293 K. This increase was attributed to the increase in the yield strength of the TiNi fibers as well as the shape memory effect of the TiNi fibers, which generates compressive stresses in the matrix when rearranging the martensitic variants after heating. In addition, the composites have higher specific strengths than AZ31 Mg alloy at temperatures higher than 373 K, suggesting that $TiNi_f$ reinforced AZ31 Mg alloy composites have significant potential for high-temperature applications.

5.1.3. Compression properties

Table 7 provides a comprehensive summary of the mechanical properties of Mg-Ti composites under compression testing, highlighting the influence of various fabrication methods, matrix materials, reinforcement types, and processing parameters. The matrix materials primarily include pure Mg and AZ31 Mg alloy, while the reinforcements vary from titanium

Table 6
Summary of the mechanical properties under tension testing at elevated temperature of Mg-Ti composites corresponding various fabrication methods.

Matrix	Reinforcement	Method	Technological parameter	Temp.	Mechanical properties			Ref.
					YS (MPa)	UTS (MPs)	EL (%)	
Mg	10 vol.%Tip	PM	Milling: 100 rpm; 1 h;	25 °C	–	158	7.8	[149]
		Hot extrusion	Encapsulated extrusion:	100 °C	–	77	8.3	
			400 °C/18:1	200 °C	–	41	12.7	
				300 °C	–	25	14.7	
AZ31	5 at.%Tip	PM	Uniaxially hot compacted:	25 °C	240	322	16.3	[81]
	10 at.%Tip		50 MPa; 250 °C/30 min;		280	365	16.1	
	15 at.%Tip	Hot extrusion	Extrusion: 250 °C/10.6:1		341	512	15.8	
	5 at.%Tip			300 °C	56	63	11.4	
	10 at.%Tip				58	69	11.8	
	15 at.%Tip				63	82	12.1	
AZ31	–	Pulsed current	Pressed: 32 MPa; heating	20 °C	190	185	–	[67]
	20 vol.%TiNif	hot pressing	rate of 1.7 K/s at a holding		194	193	6.8	
	–		temperature of 773 K;	100 °C	169	185	–	
	20 vol.%TiNif		5 min; a vacuum of 2 Pa.		178	262	7.9	
	–			150 °C	136	150	–	
	20 vol.%TiNif				281	302	20.4	

Table 7
Summary of the mechanical properties under compression testing of Mg-Ti composites corresponding various fabrication methods.

Matrix	Reinforcement	Method	Technological parameter	Mechanical properties			Ref.
				YS (MPa)	UCS (MPs)	EL (%)	
Mg	–	DMD	Slurry: stirred at 460 rpm for	86±1	326±1		[138,139]
			8 min;			20.8±1.7	
	0.58 vol.%Tip		Ar gas flow rate: 25 L/min;	129±2	431±8		
		Hot extrusion	Hot extrusion: 350 °C/ 20.25:1			17.4±0.3	
	0.97 vol.%Tip			130±8	413±15		
						18.5±0.6	
	1.98 vol.%Tip			120±5	415±4		
						17.1±0.8	
	5.6 vol.%Tip			85±3	360±5		
						13.6±1.2	
Mg	–	DMD	Slurry: stirred at 450 rpm for	46±2	274±4		[140]
			5 min;			23.0±0.9	
	0.5 wt.%NiTip		Ar gas flow rate: 25 L/min;	42±4	265±15		
		Hot extrusion	Hot extrusion: 350 °C/ 20.25:1			23.0±0.3	
	1 wt.%NiTip			52±6	290±4		
						23.0±0.7	
	1.5 wt.%NiTip			78±5	337±4		
						18.0±0.4	
	3 wt.%NiTip			94±3	345±5		
						18.0±0.9	
Mg	–	Rotary hot	Vessel: 450 °C for 10 min;	130	270	14.4	[150]
	5 vol.%TiNip	swaging	Deformation: ~45%;	145	320	15.2	
	10 vol.%TiNip	Annealing	Annealing: 600 °C for 90 min	148	312	14.4	
	15 vol.%TiNip			150	335	14.8	
Mg	–	PM	Milling time: 3 h;	128	403	21	[141]
	3 mass.%Tip		Spark plasma sintering:	130	410	17.5	
	5 mass.%Tip		30 MPa; 600 °C/30min;	135	418	16.5	
		Hot extrusion	Hot extrusion: 400 °C/37.7:1				
AZ31	5 at.%Tip	PM	Uniaxially hot compacted:	229	374	16.3	[81]
	10 at.%Tip		50 MPa; 250 °C/30 min;	276	420	16.0	
	15 at.%Tip	Hot extrusion	Hot extrusion: 250 °C/10.6:1	341	512	15.8	
AZ31	–	PM	Milling: 200 rpm, 110 h;	99	307	19.6	[151]
	9 wt.%Tip	Cold pressing	Cold press: 1500 MPa	293	325	10.4	
	18 wt.%Tip			312	332	11.1	
	27 wt.%Tip			336	361	9.5	

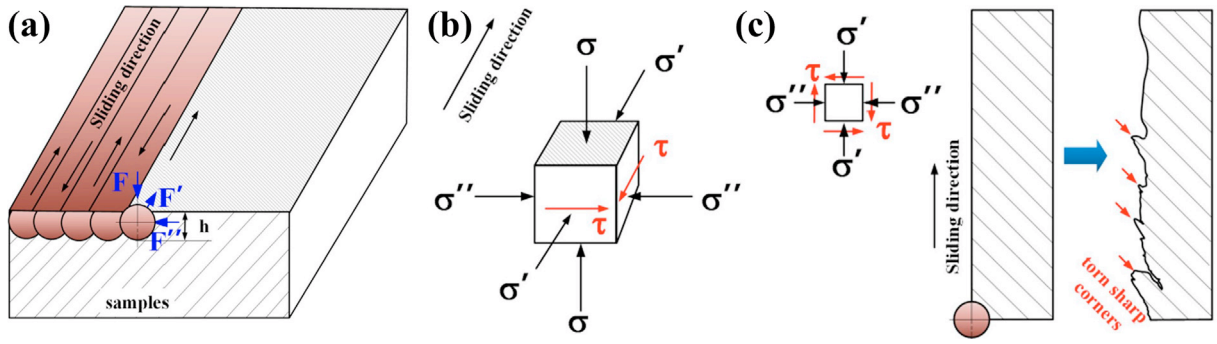

Fig. 21. Schematic of the sliding friction of the matrix and Ti-reinforced composites: (a) sliding friction process; (b) stress element during sliding; (c) stress on sliding plane and possible friction mechanism [76].

particles (Tip) to Ni-Ti composite particles (NiTip) and Ti-Ni intermetallic compounds (TiNip). Fabrication methods encompass diffusion molten deposition (DMD), rotary hot swaging, and powder metallurgy (PM), often combined with subsequent processes such as hot extrusion, cold pressing, or annealing.

The results demonstrate that the addition of reinforcements significantly enhances the yield strength (YS) and ultimate compressive strength (UCS) of the composites, albeit often at the expense of elongation (EL). For instance, in pure Mg matrices processed via DMD and hot extrusion, increasing Tip content from 0.58 vol.% to 5.6 vol.% initially improves YS and UCS but eventually leads to a decline in EL. Similarly, NiTip reinforcements exhibit a progressive increase in YS and UCS with higher content, though EL decreases beyond a certain threshold. The addition of 15 at.%Ti particles to AZ31 alloy in PM and hot extension preparations resulted in the best ultimate compressive strength, yield strength, and elongation of 512 MPa, 341 MPa, and 15.8%, respectively [81]. Good plasticity was obtained through different preparation processes and different additions of Ti particles, TiNi, and NiTi particles.

The data underscore the critical role of reinforcement type, content, and processing parameters in tailoring the mechanical performance of Mg-Ti composites, offering valuable insights for the development of lightweight, high-strength materials for structural applications.

5.1.4. Tribological property

Beyond overall strength, surface mechanical attributes, such as resistance to scratching and wear, are vital in numerous engineering applications [152–154]. Repeated shear stress during reciprocating friction promotes the development of sharp edges, which may break away as wear debris. As illustrated in Fig. 21, the sliding friction process involves complex force interactions, including compressive loads, shear traction, and squeezing actions [76]. Conventional surface treatments, such as hydrothermally-applied coatings, have limited effectiveness in enhancing the hardness and wear resistance of Mg alloys due to the poor bonding interfaces formed with the Mg matrix [155]. Thus, considerable attention has been directed toward establishing strong interfacial bonds between the Mg matrix and surface coatings to simultaneously enhance hardness and wear resistance in MMCs. In usual, extensive research has already focused on ceramic reinforcements for enhancing the hardness and wear resistance of MMCs, with B_4C and SiC identified as the most commonly used reinforcements [156]. In contrast, studies on the use of Ti particles as reinforcement are still emerging. Owing to their exceptional strength-to-weight ratio and corrosion resistance, play a significant role. Dispersing Ti particle within the Mg matrix composites restricts dislocation mobility, thereby enhancing MMCs strength and improving wear resistance by evenly redistributing the applied stresses [145,147].

As depicted in Fig. 22a, optimizing the Ti content is essential for enhancing the tribological performance of the Ti/AZ31 composite. The presence of Ti particles has a significantly impact on the friction and wear behavior of these composite. Specifically, the coefficient of friction (COF) decreases from 0.293 to 0.261 as the Ti content increases to 6 wt.%, suggesting improved sliding performance. However, further addition of Ti results in a slight increase in the COF, which rises to 0.272 [94]. Similarly, the wear track width initially reduces, reaching a minimum before expanding at higher Ti contents, while the wear depth consistently decreases as Ti content increases. These trends highlight the role of Ti particles in enhancing wear resistance, although their effect diminishes once the Ti content exceeds a certain threshold. In terms of the wear rate, the running-in period typically shows a higher rate of wear compared to the steady-state phase. Consequently, a shorter running-in period contributes to improved overall wear resistance of the Ti/AZ91 composite [157], as depicted in Fig. 22b_2. Furthermore, Ti particles significantly improve wear resistance under varying loading forces, as shown in Fig. 22$c_{1\text{-}2}$. Notably, at a load of 300 N, the wear rate of the base alloy is nearly three times higher than that of the 5 vol.% TC4/AZ91D composite (Fig. 22c_4) [47].

The COF results of Tip-reinforced Mg-RE composites are depicted in Fig. 22d-e. The COF curves indicate that the Mg-RE matrix, characterized by its relatively lower strength, is more susceptible to corner tearing under shear forces compared to Ti-reinforced composites. This observation underscores the contribution of Ti particles to enhancing wear resistance of MMCs. As illustrated in Fig. 22d_5, and d_7, the wear depth of the matrix is greater than that of the composite,

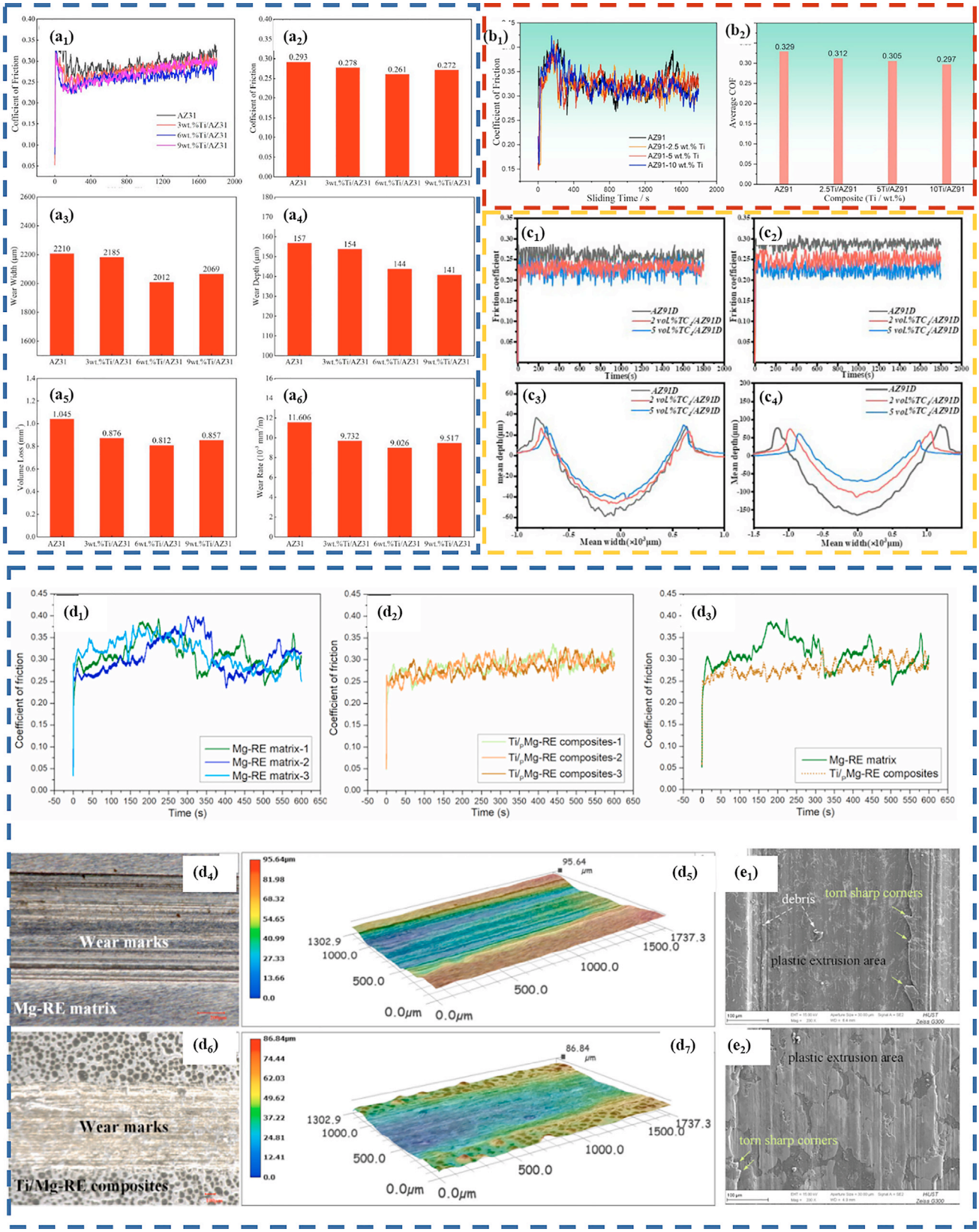

Fig. 22. Coefficients of friction (COF) of the Mg matrix and Tip/Mg composites. (a_1-a_6) Three repeated results of the AZ31 matrix and Ti/AZ31 composite [94], (b_1-b_2) repeated results of the AZ91 matrix and Ti/AZ91 composite [157]; (c_1, c_2) friction coefficients of TC4/AZ91D under 150 N and 300 N loads; (c_3, c_4) cross-sectional profiles under 150 N and 300 N loads [47]; COF of the Mg-RE matrix and Ti_P/Mg-RE composites: (d_1-d_3) three repeated results of the Mg-RE and the Tip/Mg-RE composites, (d_4-d_7) worn surface morphologies and 3D measurements after friction tests; (e_1, e_2) SEM images showing worn surfaces of Mg-RE alloy and Ti_P/Mg-RE composites [45].

further supporting the superior frictional resistance of Tip/Mg-RE composites. The increased loading results in higher roughness across all composites, with the roughness primarily due to material loss from the surface, leading to greater surface irregularities [158]. Notably, the pressure resistance of the Mg matrix decreases as the load increases during the wear process. Fig. 22e_1, and e_2 highlights that the ploughing occurred in the matrix region, where Ti particles were absent, whereas Mg-RE matrix exhibited a more pronounced plowing effect. Both samples exhibited the peeling of debris and the formation of pits during the wear process; however, the pit area in the Mg-RE alloy was larger than in the composite. Additionally, sharp torn corners were observed in both, with more pronounced tearing in the Mg-RE alloy. To sum up, the Ti-particle reinforced Mg-RE composites demonstrate a lower friction coefficient compared to the Mg-RE matrix, and the COF increases progressively with the sliding distance.

5.2. Physical properties

While much of the research on MMCs primarily focuses on their mechanical properties, there is relatively limited studies address the physical properties, such as thermal conductivity [159,160], electromagnetic shielding [161], and corrosion resistance [162,163].

5.2.1. Thermal conductivity

Research has explored the trade-off between strength and thermal conductivity in Mg alloys by strengthening mechanisms, including grain refinement, solid solution, dislocation, and diffusion strengthening, which generally decrease thermal conductivity [164]. Huang et al. [165] reinforced a WE43 alloy matrix with 7 wt.%Mn3Ga0.7Ge0.3N particles. The strong interaction between magnetism and elasticity within the anti-calcite particles, including the electron spin modulation of Mn atoms, resulted in a high mechanical property and exhibited a coefficient of thermal expansion 22.7 $\times$ 10^{-6} K^{-1}. Recent researches have focused on using high-strength Mg RE alloys as matrix, reinforced with Ti particles, to improve both strength and thermal conductivity in comparison to the unreinforced alloys. For example, Wang et al. [166] reported that the 6Tip/WE43 composite exhibited a maximum thermal conductivity of 83 $Wm^{-1}K^{-1}$ at 200 °C, along with high tensile strength and good ductility, as shown in Fig. 23a. Furthermore, Luo et al. [157] investigated the effect of introducing of Ti particles and optimizing thermal comprehensive deformation processes—specifically, extrusion followed by hot rolling (as shown in Fig. 23b)—on the 2.5 wt.%Ti/AZ91 composite. Their results showed a significant enhancement in thermal conductivity, achieving 100.1 $Wm^{-1}K^{-1}$ at 200 °C and an increase in room temperature thermal conductivity to 63.8 $Wm^{-1}K^{-1}$. This thermal conductivity substantially exceeded that of the AZ91 alloy, which had a reported thermal conductivity of 51.2 $Wm^{-1}K^{-1}$. These researches highlight the potential for tailored reinforcement strategies to simultaneously enhance the mechanical and thermal properties of MMCs.

5.2.2. Electromagnetic shielding

Electromagnetic shielding (EMS) can effectively protect electronic equipment from severe electromagnetic interference and radiation [91,167], and has garnered significant attention in recent years. Mg alloys and MMCs are the potential materials for electromagnetic shielding because Mg alloys and composites are lighter in weight compared to other shielding metals at the same thickness. Pandey et al. [168] introduced Ti particles into the Mg matrix and investigated that the average electromagnetic shielding effectiveness of the Mg-Ti microcomposite was increased by nearly 9% compared to pure Mg in the same frequency range. Fig. 24a presents a schematic that illustrates how Ti particles contribute to the overall mechanism of electromagnetic wave attenuation. Fig. 24b illustrated that Mg/15Ti exhibits the highest absorption performance in the X-band microwave range. The Ti particles, characterized by lower geometrical symmetry and higher aspect ratios, enhance the absorption and multiple reflections of electromagnetic waves, leading to greater attenuation of their intensity, making them more effective as absorbers than reflectors. Fig. 24c-d illustrated that the SnO_2-coated graphene oxide (GO) reinforced AZ31 MMCs show better EMI (electromagnetic interference) shielding performance than AZ31 alloy in the range of 200–1400 MHz and the X-band [169].

5.2.3. Corrosion resistance

The corrosion resistance of Ti reinforced MMCs has garnered extensive attention in high-performance engineering applications, including biomedical implants, aerospace skin panels, and automotive transmission components [170,171]. Jiao et al. [172] fabricated Ti/AZ31 MMCs via powder metallurgy, incorporating 1.5 wt.% and 5 wt.% nano-Ti particles alongside 10 wt.% micro-Ti particles. As shown in Fig. 25a, both the AZ31 alloy and composites exhibited progressive mass loss with prolonged immersion time, with the composites consistently demonstrating higher corrosion rates than the monolithic alloy. Moreover, hydrogen evolution tests revealed that after approximately 30 h of immersion, the corrosion rate followed the trend: 1.5% Ti/AZ31 < 10% Ti/AZ31. Conversely, mass-loss measurements displayed the inverse relationship: 1.5% Ti/AZ31 > 10% Ti/AZ31. In addition, severe galvanic corrosion occurs between Ti and the Mg matrix. The Ti particles, distributed along the interfaces of the original AZ31 powder particles, form a discontinuous network structure. As illustrated in schematic Fig. 25b, when the composite is exposed to the corrosive medium, the low-Al-content regions adjacent to Ti particles corrode preferentially. Subsequently, the corrosion propagates continuously along the interfaces where Ti particles are distributed within the matrix.

The effects of Ti particles and TC4 particles on the corrosion behavior of AZ91D MMCs was systematically investigated in 3.5% NaCl solution [170]. As illustrated in Fig. 25c and d, the significant potential difference between Ti/TC4 particles and the AZ91D matrix makes them primary sites for cathodic hydrogen evolution, thereby markedly accelerating galvanic corrosion in magnesium matrix composites, with the AZ91D-Ti couple exhibiting a higher corrosion in-

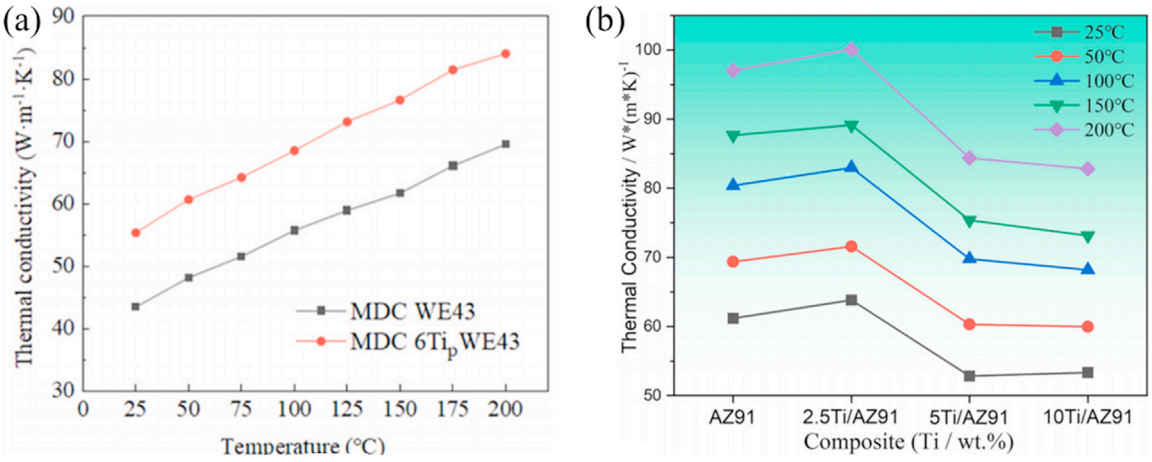

Fig. 23. Thermal conductivity of the (a) MDC WE43 and 6Tip/WE43 [166]; the (b) xTi/AZ91 (x = 0, 2.5, 5, and 10 wt.%) [157].

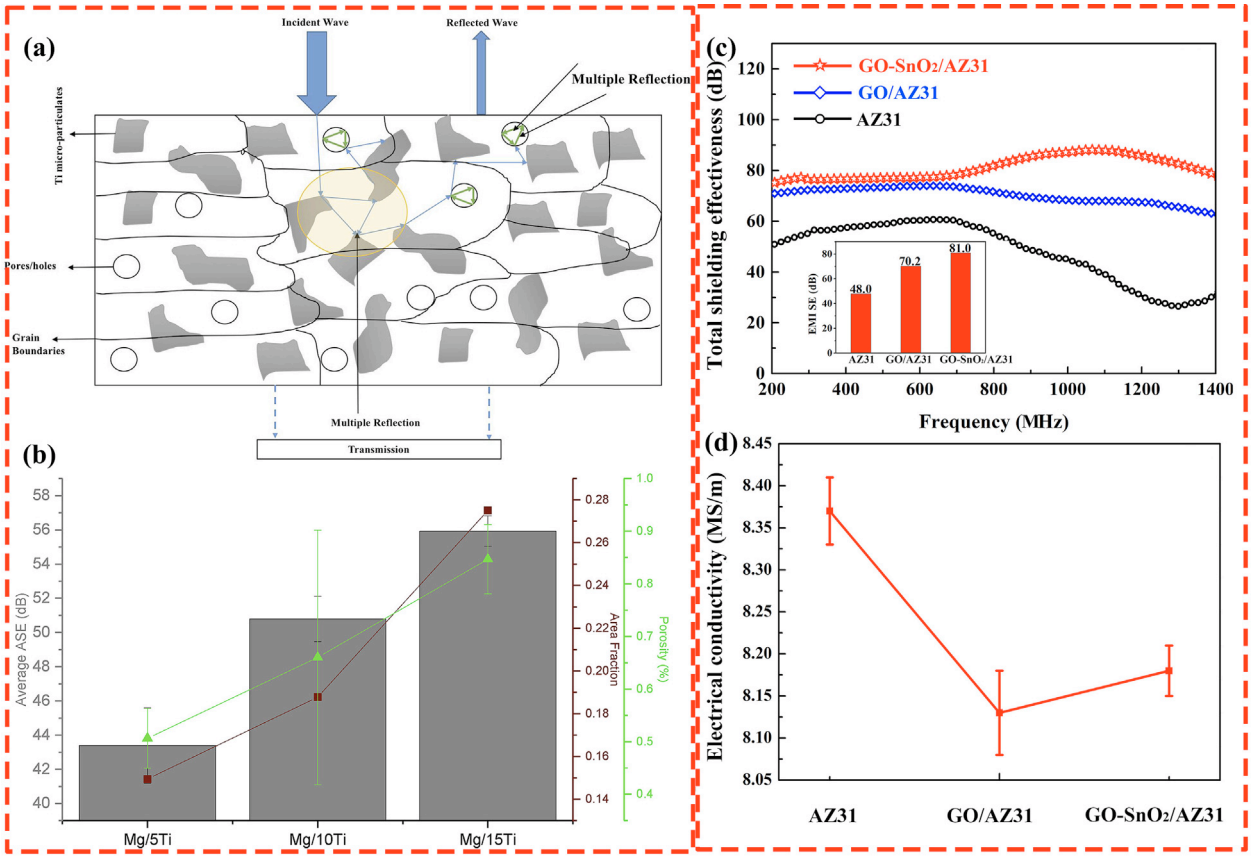

Fig. 24. Electromagnetic interference shielding properties of Mg and its composites. (a) Mechanisms of electromagnetic wave attenuation through reflection, absorption, and multiple reflections; (b) influence of Ti micro-reinforcements and porosity on absorption effectiveness [168]; (c) shielding performance from 200 MHz to 1400 MHz of AZ31 and its composites; (d) X-band shielding performance [169].

tensity than AZ91D-TC4. Notably, under hydrogen evolution corrosion conditions, an elevated hydrogen overpotential directly correlates with increased cathodic polarization resistance, consequently diminishing corrosion rates [173]. Crucially, Ti demonstrates superior hydrogen evolution reactivity relative to TC4 [174], accounting for the attenuated corrosion rate observed in TC4/AZ91D composites (38.27 mm/year) versus Ti/AZ91D (49.13 mm/year). With escalating TC4 particle concentrations, a proliferation of micro-electrochemical cells ensues, precipitating particle mobilization and subsequent formation of bifurcated erosion pathways [47]. Collectively, these results elucidate the critical influence of reinforcement composition, concentration, and microstructural arrangement on the corrosion mechanisms and electrochem-

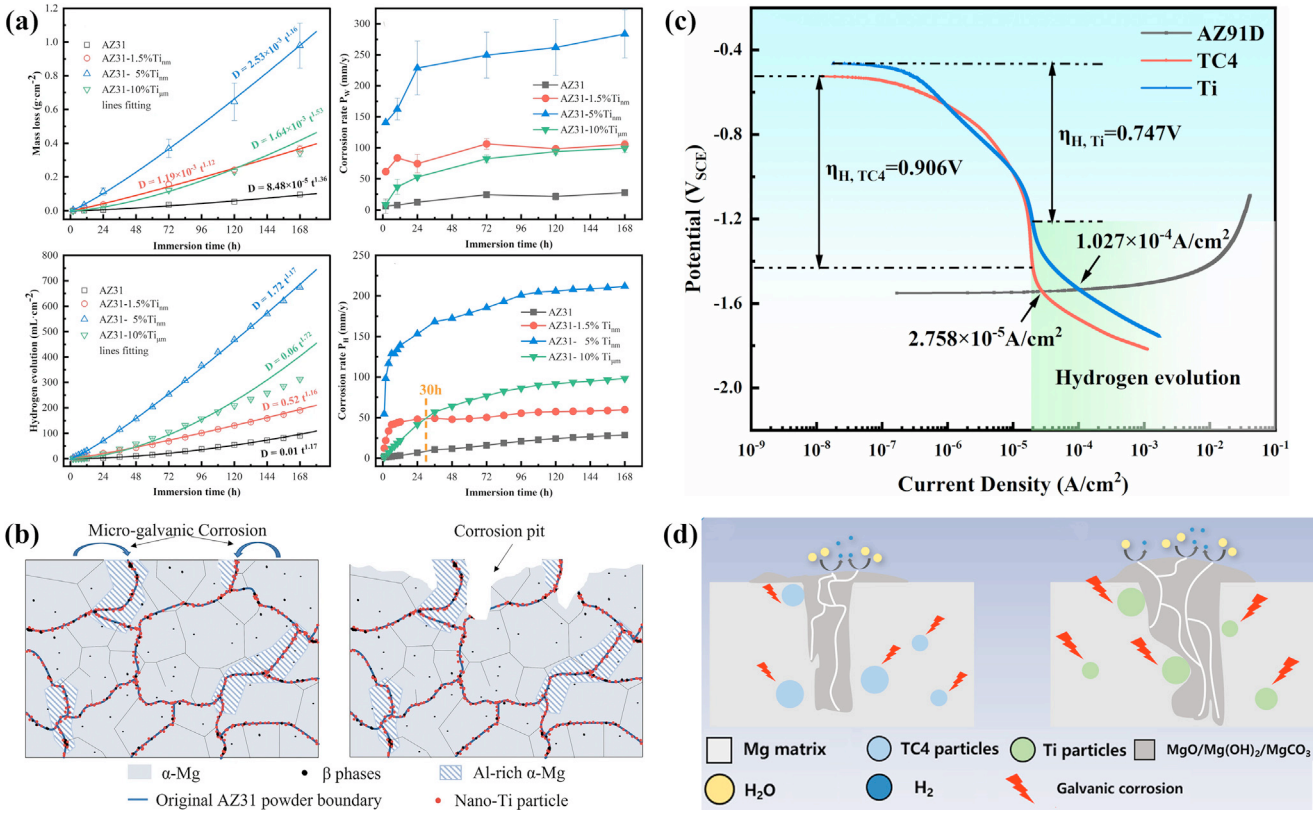

Fig. 25. Corrosion resistance of AZ alloy and composites. (a) Immersion test result and (b) schematic illustration of the corrosion mechanism for the Ti/AZ31 composite [172]; (c) anodic polarization curves of AZ91D and cathodic polarization curves of Ti/TC4 composites; (d) schematic diagram of corrosion mechanism of composites TC4/AZ91D and Ti/AZ91D [170].

ical stability of Ti and TC4 reinforced MMCs, providing a scientific basis for their tailored optimization in advanced engineering applications.

6. Summary and outlook

Magnesium matrix composites (MMCs) are gaining increasing attention due to their unique combination of low density, high specific strength, and high specific modulus, making them suitable for applications in aerospace, automotive, and electronics industries. Recent research has demonstrated that incorporating deformable Ti reinforcements can significantly enhance the properties of MMCs. In this review, we briefly introduce the main preparation methods for Ti-Mg composites and systematically summarize advances in Ti-Mg composites, focusing on factors affecting their mechanical performance.

Studies reveal that deformation incompatibility between the Ti and Mg phases induces significant strain gradients and accumulates geometrically necessary dislocations (GNDs) at the heterointerface, driving higher hetero-deformation-induced (HDI) strengthening, increased Mg non-basal slip activity, and improved ductility of Ti-Mg laminates. Various Mg alloy matrices have been used, including commercial AZ (Mg-Al-Zn), AM (Mg-Al-Mn), and VW (Mg-RE-Zn) series. Progress has been made in characterizing the interfacial reaction products between the Mg matrix and Ti reinforcements. Additionally, the inclusion of Ti not only strengthens the composite but also impacts tribological behavior, thermal conductivity and corrosion resistance, highlighting its multifunctional benefits.

Despite these achievements, several significant gaps remain in Ti-Mg composite research:

(1) Understanding Interfacial Structure-Property Relationships: The impact of the morphology and size of interfacial reaction products on interfacial bonding strength is not yet fully understood. While substantial progress has been made in characterizing the interfacial reaction products that form between the Mg matrix and Ti reinforcements, several critical issues remain unresolved. The effects of alloying elements like Al, Mn, and Zr introduce extra complexity and tuning potential for interfacial structures. Further research is required to clarify how these elements and surface modification methods modulate interfacial products and thus influence both bonding and overall mechanical properties. Systematic study of these relationships is crucial for advancing the design and performance of Mg matrix composites.

(2) Constitutive Modeling: Current micromechanical constitutive models are insufficient for accurately describing the deformation behavior of Ti-Mg composites, as they rarely account for the distinct plasticity and phase inter-

actions of Ti and Mg. Developing sophisticated, phase-specific constitutive models is crucial for guiding the microstructural design and optimizing processing parameters.

(3) Physical Properties and Functional Performance: The addition of Ti reinforcement not only enhances the mechanical properties of MMCs but also significantly affects their tribological wear, thermal conductivity and corrosion resistance. Compared to research on mechanical properties and strengthening–toughening mechanisms, studies on the functional characteristics of Ti-reinforced Mg-based composites—such as wear resistance, thermal conductivity, and other physical properties—are still in their infancy. The influence of Ti reinforcement on these functional attributes remains insufficiently explored. In particular, there is a need for a deeper understanding of how second phase size, texture, and grain structure govern these functional properties, to guide further optimization and application development.

Looking ahead, outstanding properties of Ti-reinforced MMCs—such as low density, high specific strength, and excellent corrosion resistance—show great potential for future applications in emerging fields. With the rapid development of the low-altitude economy, there is a growing demand for lightweight and high-performance structural materials in areas such as unmanned aerial vehicles (UAVs) and urban air mobility (UAM). Ti-reinforced MMCs are expected to play a vital role in these areas. With continued progress in interface engineering, mechanism research, and material design, these composites will likely demonstrate significant application value in key equipment used in the low-altitude economy, providing a solid technical foundation for the advancement of new materials in this domain.

Declaration of competing interest

The authors declare that they have no known competing financial interests or personal relationships that could have appeared to influence the work reported in this paper.

CRediT authorship contribution statement

Yitao Wang: Writing – original draft, Investigation, Data curation, Conceptualization. **Jianbo Li:** Resources, Project administration. **Huan Luo:** Data curation. **Weizhang Wang:** Investigation. **Daiyi Deng:** Data curation. **Jianwei Chen:** Investigation. **Xianhua Chen:** Funding acquisition. **Kaihong Zheng:** Supervision. **Fusheng Pan:** Supervision.

Acknowledgments

The authors express their sincere thanks for the financial support from the National Key R&D Program of China (No. 2022YFB3708400), National Natural Science Foundation of China (No. 52171133, 52225101), Basic and Applied Basic Research Foundation of Guangdong (No. 2020B0301030006).

References

[1] C.M. Cepeda-Jiménez, et al., Acta Mater 108 (2016) 304–316.
[2] J. Wang, et al., Acta Mater 217 (2021) 117151.
[3] S. Ouyang, et al., Scr. Mater. 213 (2022) 114598.
[4] S. Lyu, et al., Mater. Sci. Eng.: A 856 (2022) 143783–143792.
[5] A.A. Luo, J. Magnes. Alloy. 13 (1) (2025) 1–3.
[6] W. Zhang, et al., Mater. Des. 221 (2022) 110994.
[7] Y. Yang, et al., J. Magnes. Alloy. 9 (3) (2021) 705–747.
[8] A. Koushki, et al., Mater. Sci. Eng.: A 889 (2024) 145764.
[9] M.S. Mehranpour, et al., Mater. Sci. Eng.: A 802 (2021) 140667.
[10] Y. Zhang, et al., J. Mater. Sci. Technol. 51 (2020) 102–110.
[11] K. Xue, et al., Mater. Sci. Eng.: A 891 (2024) 145953.
[12] W.T. Sun, et al., Acta Mater 151 (2018) 260–270.
[13] X. Qi, et al., J. Mater. Sci. Technol. 166 (2023) 123–132.
[14] Z. Yu, et al., Scr. Mater. 220 (2022) 114901.
[15] J. Sun, et al., Nanomed. Nanotechnol. Biol. Med. 10 (10) (2022) 2649–2672.
[16] H.T. Guan, et al., Nanotechnol. Rev. 11 (1) (2022) 712–730.
[17] K.K. Deng, et al., Acta Metall. Sin. (Engl. Lett.) 32 (4) (2019) 413–425.
[18] M. Haghshenas, J. Magnes. Alloy. 5 (2) (2017) 189–201.
[19] K.B. Nie, et al., J. Mater. Res. 32 (13) (2017) 2609–2620.
[20] P. Xiao, et al., Compos. B. Eng. 198 (2020) 108174–108188.
[21] D.S. Kumar, et al., Can. Metall. Q. 59 (3) (2020) 316–323.
[22] Y. Li, et al., Adv. Eng. Mater. 20 (7) (2018) 1800131.
[23] S.K. Sahoo, et al., Compos. B. Eng. (2022) 110476.
[24] L. Xi, et al., J. Magnes. Alloy. (2025).
[25] C. Wang, et al., J. Magnes. Alloy. (2024) 1294–1309.
[26] X. Zhang, et al., J. Magnes. Alloy. (2024).
[27] H. Yang, et al., J. Magnes. Alloy. 10 (9) (2022) 2311–2333.
[28] S.F. Hassan, et al., J. Mater. Sci. 37 (12) (2002) 2467–2474.
[29] D.R. Ni, et al., Acta Metall. Sin. (Engl. Lett.) 27 (5) (2014) 739–761.
[30] S.F. Hassan, et al., Mater. Res. Bull. 37 (2) (2002) 377–389.
[31] Z.Y. Xu, et al., Compos. B. Eng. 242 (2022) 110069.
[32] X. Chen, et al., J. Magnes. Alloy. (2024) 15836.
[33] S.F. Hassan, et al., J. Alloys Compd. 345 (1) (2002) 246–251.
[34] K.N. Braszczynska-Malik, Materials (Basel) 14 (18) (2021) 5182.
[35] S.S.d. Rocha, et al., Braz. Dent. J. 17 (2006) 126–129.
[36] D. Li, et al., Acta Mater 206 (2021) 116627.
[37] A.H. Yusop, et al., Int. J. Biomater. 2012 (2012) 641430.
[38] L. Lei, et al., Mater. Sci. Eng.: A 801 (2021) 140411.
[39] Y.L. Zhou, et al., Mater. Sci. Eng.: A 371 (1) (2004) 283–290.
[40] M. Niinomi, Mater. Sci. Eng.: A 243 (1–2) (1998) 231–236.
[41] Q.S. Mei, et al., Scripta Mater 63 (10) (2010) 977–980.
[42] Y. Chen, et al., Shape Mem. Superelasticity 5 (2019) 42–62.
[43] C. Jiang, et al., J. Magnes. Alloy. 12 (12) (2024) 4768–4807.
[44] D.K. Sharma, et al., Mater. Today Proc 26 (2020) 506–519.
[45] A.S.A. Tallam, et al., Int. J. Interact. Des. Manuf. (2025) 1–20.
[46] K. Nie, et al., Mater. Sci. Eng.: A 528 (29–30) (2011) 8709–8714.
[47] Z. Yu, et al., J. Mater. Res. Technol. 26 (2023) 7395–7411.
[48] K. Nie, et al., J. Alloys Compd. 509 (35) (2011) 8664–8669.
[49] D. Pu, et al., Mater. Sci. Eng.: A 858 (2022) 144140.
[50] J.-h. Zhao, et al., Trans. Nonferrous Met. Soc. China 32 (4) (2022) 1144–1158.
[51] T.Satish Kumar, et al., Sci. Rep. 14 (1) (2024) 26686.
[52] Y.-b. WU, et al., Trans. Nonferrous Met. Soc. China 34 (3) (2024) 846–860.
[53] G. Cheng, et al., Spec. Cast. Nonferrous Alloys 42 (6) (2022) 681–687.
[54] K. He, et al., Mater. Des. 112 (2016) 553–564.
[55] F. Wen, et al., Met Mater Int 28 (7) (2021) 1711–1724.
[56] Z. Li, et al., J. Mater. Process. Technol. 331 (2024) 118509.
[57] X. Han, et al., J. Mater. Res. Technol. 29 (2024) 3192–3204.

[58] A. Bahrami, et al., Crit. Rev. Environ. Sci. Technol. 46 (2) (2016) 143–208.
[59] M. Çelebi, et al., Adv. Powder Technol. 36 (4) (2025) 104835.
[60] M. Çelebi, et al., Powder Technol 449 (2025) 120439.
[61] A. Çanakçı, et al., Arabian J. Sci. Eng. 49 (11) (2024) 14625–14641.
[62] M. Çelebi, et al., JOM 75 (9) (2023) 3935–3950.
[63] Y.Z. Zhang, et al., J. Mater. Res. Technol. 30 (2024) 3152–3177.
[64] B. Tang, et al., Acta Metall. Sin. (Engl. Lett.) 35 (12) (2022) 1935–1945.
[65] Y. Wang, et al., Mater. Sci. Eng.: A 900 (2024) 146490.
[66] X. Cai, et al., Compos. B. Eng. 215 (2021) 108743.
[67] K. Mizuuchi, et al., Mater. Sci. Eng.: A 367 (1–2) (2004) 343–349.
[68] M. Çelebi, et al., JOM 74 (11) (2022) 4449–4461.
[69] L. Yang, et al., J. Alloys Compd. 870 (2021) 159473.
[70] K. Kitazono, et al., Mater Trans 52 (2) (2011) 155–158.
[71] B. Alobaid, Metallogr. Microstruc. 11 (5) (2022) 761–773.
[72] Y. Feng, et al., Mater. Sci. Eng.: A 888 (2023) 145783.
[73] K. Kitazono, et al., Mater. Sci. Forum 735 (2013) 87–92.
[74] L. Sun, et al., Mater. Today Commun. 43 (2025) 111638.
[75] V. Sivaramakrishnan, et al., J. Manuf. Eng. 12 (1) (2017) 041–048.
[76] Z. Gui, et al., Mater. Sci. Eng. B 287 (2023) 116095.
[77] L. Li, et al., Surf. Coatings Technol. 385 (2020) 125371.
[78] R.V. Marode, et al., J. Magnes. Alloy. 12 (6) (2024) 2091–2146.
[79] I. Dinaharan, et al., J. Alloys Compd. 820 (2020) 153071.
[80] N. Gangil, et al., Metals (Basel) 10 (11) (2020) 1425.
[81] H. Yu, et al., Adv. Powder Technol. 29 (12) (2018) 3241–3249.
[82] D. Peng, et al., J. Magnes. Alloy. (2025).
[83] C. Fuentes, et al., Colloids Surf. Physicochem. Eng. Aspects 558 (2018) 280–290.
[84] A. Mortensen, et al., Int. Mater. Rev. 37 (1) (1992) 101–128.
[85] K. Kondoh, et al., Acta Mater 58 (2) (2010) 606–614.
[86] D. Muscat, et al., Metall. Mater. Trans. A 25 (1994) 2357–2370.
[87] M. Razzaghi, et al., Compos. B. Eng. 190 (2020) 107947.
[88] D. Zhang, et al., Appl. Surf. Sci. 256 (23) (2010) 7043–7047.
[89] D. Zhang, et al., Mater. Chem. Phys. 130 (1–2) (2011) 665–671.
[90] J.P. Xiong, et al., Cailiao Gongcheng-J Mater Eng 51 (1) (2023) 1–15.
[91] Z.Y. Xu, et al., J. Magnes. Alloy. (2024).
[92] L. Bao, et al., J. Mater. Sci. Technol. (2022) 197–206.
[93] R. Wang, et al., Materials (Basel) 15 (20) (2022) 7075.
[94] J. Ye, et al., J. Magnes. Alloy. 10 (8) (2022) 2266–2279.
[95] J. Ye, et al., Vacuum 203 (2022) 111287.
[96] H. Luo, et al., Mater. Charact. 191 (2022) 112154.
[97] X. Li, et al., Mater. Sci. Eng.: A 765 (2019) 138283.
[98] B. Tang, et al., Vacuum 206 (2022) 111534.
[99] H. Wang, et al., Mater. Charact. 207 (2024) 113526.
[100] N. Li, et al., Scripta Mater. 227 (2023) 115278.
[101] H. Luo, et al., Mater. Sci. Eng.: A 886 (2023) 145723.
[102] J. Ye, et al., Mater. Sci. Eng.: A 833 (2022) 142526.
[103] Y. Xu, et al., Adv. Eng. Mater. 26 (6) (2024) 2301349.
[104] G. Chen, et al., J. Mater. Res. Technol. 29 (2024) 3494–3507.
[105] X.M. Wang, et al., Acta Metall. Sin. (Engl. Lett.) 29 (10) (2016) 940–950.
[106] Y. Zhang, et al., J. Mater. Res. Technol. 30 (2024) 5711–5723.
[107] Y. Zhang, et al., Compos. Part A-Appl. S. 185 (2024) 108376.
[108] X. Sun, et al., J. Alloys Compd. 727 (2017) 1263–1272.
[109] W. Zhao, et al., J. Magnes. Alloy. 12 (4) (2024) 1511–1517.
[110] Y.D. Fan, et al., Mater. Sci. Eng.: A 833 (2022) 142336.
[111] W. Ai, et al., Mater. Sci. Eng.: A 850 (2022) 143560.
[112] X. Chen, et al., J. Mater. Sci. Technol. 185 (2024) 69–82.
[113] Y. Wang, et al., Mater. Sci. Eng.: A 856 (2022) 144017.
[114] D. Pu, et al., Mater. Sci. Eng.: A 879 (2023) 145278.
[115] D. Pu, et al., J. Mater. Res. Technol. 22 (2023) 1362–1374.
[116] W. Wang, et al., Mater. Sci. Eng.: A 892 (2024) 146067.
[117] W. Wang, et al., Mater. Sci. Eng.: A 862 (2023) 144377.
[118] X.-L. Nan, et al., Scripta Mater 67 (5) (2012) 443–446.
[119] D. Xia, et al., Scripta Mater 171 (2019) 31–35.
[120] R. Xin, et al., Scripta Mater 74 (2014) 96–99.
[121] C. Xie, et al., J. Magnes. Alloy. 12 (7) (2024) 2967–2984.
[122] J. Lee, et al., J. Magnes. Alloy. 12 (8) (2024) 3409–3430.
[123] X. Zhang, et al., J. Magnes. Alloy. 13 (6) (2024) 2800–2812.
[124] C. Liu, et al., J. Magnes. Alloy. (2024).
[125] C. Yu, et al., Int. J. Solids Struct. 170 (2019) 38–52.
[126] H. Zhang, et al., J. Alloys Compd. 999 (2024) 175047.
[127] D.-g. Fan, et al., J. Mater. Res. Technol. 10 (2021) 422–437.
[128] J. Long, et al., J. Magnes. Alloy. 12 (7) (2024) 3003–3023.
[129] L. Han, et al., J. Magnes. Alloy. 12 (7) (2024) 2890–2908.
[130] B.K. Raghunath, et al., Mater. Des. 29 (3) (2008) 622–627.
[131] X. Chen, et al., J. Mater. Res. Technol. 24 (2023) 200–214.
[132] S. Sankaranarayanan, et al., Mater. Des. 37 (2012) 274–284.
[133] C.-j. Wang, et al., J. Magnes. Alloy. 13 (6) (2024) 4050–4054.
[134] W. Wang, et al., Rare Met. Mater. Eng. 49 (12) (2020) 4050–4054.
[135] F. Cao, et al., Mater. Sci. Eng.: A 891 (2024) 145981.
[136] F. Aydın, Mater. Sci. Technol. 40 (5) (2024) 339–376.
[137] F. Aydin, J. Magnes. Alloy. 10 (10) (2022) 2673–2698.
[138] G.K. Meenashisundaram, et al., J Alloy Compd 593 (2014) 176–183.
[139] S. Sankaranarayanan, et al., Mater. Sci. Eng.: A 530 (2011) 149–160.
[140] G. Parande, et al., Metals (Basel) 8 (12) (2018) 1014.
[141] J. Umeda, et al., Mater. Chem. Phys. 123 (2–3) (2010) 649–657.
[142] M. Rashad, et al., J. Magnes. Alloy. 1 (3) (2013) 242–248.
[143] I. Dinaharan, et al., Mater. Sci. Eng.: A 772 (2020) 138793.
[144] I. Dinaharan, et al., J. Mater. Eng. Perform. 30 (4) (2021) 2899–2915.
[145] I. Dinaharan, et al., J. Magnes. Alloy. 10 (4) (2022) 979–992.
[146] J. Ye, et al., J. Magnes. Alloy. 10 (8) (2022) 2266–2279.
[147] C.-L. Zhang, et al., J. Magnes. Alloy. 4 (4) (2016) 286–294.
[148] X. Wang, et al., J. Magnes. Alloy. 8 (2) (2020) 421–430.
[149] P. Pérez, et al., Compos. Sci. Technol. 64 (1) (2004) 145–151.
[150] Z. Esen, Mater. Sci. Eng.: A 558 (2012) 632–640.
[151] H. Zhou, et al., Mater. Charact. 113 (2016) 108–116.
[152] A.M. Ralls, et al., J. Magnes. Alloy. 12 (2) (2024) 405–442.
[153] Y.L. Yin, et al., J. Magnes. Alloy. 13 (1) (2025) 379–397.
[154] S. Sinha, et al., Tribol. Int. 39 (2) (2006) 184–189.
[155] C. Brookes, et al., J. Phys. D: Appl. Phys. 5 (7) (1972) 1284.
[156] F. Aydın, Tribology-Materials, Surfaces & Interfaces 17 (4) (2023) 363–396.
[157] H. Luo, et al., J. Alloys Compd. 1002 (2024) 175506.
[158] H. Ahmadian, et al., J. Mater. Res. Technol. 31 (2024) 4088–4103.
[159] F. Meng, et al., J. Magnes. Alloy. 12 (7) (2024) 2756–2765.
[160] L. Chen, et al., J. Magnes. Alloy. 12 (9) (2024) 3717–3728.
[161] J. Li, et al., J. Magnes. Alloy. 13 (3) (2024) 1243–1257.
[162] S. Candan, et al., J. Alloys Compd. 672 (2016) 197–203.
[163] H. Choi, et al., J. Alloys Compd. 664 (2016) 25–37.
[164] H. Lv, et al., J. Magnes. Alloy. 12 (5) (2024) 1687–1708.
[165] Y. Huang, et al., Acta Mater 259 (2023) 119238.
[166] H. Wang, et al., J Alloy Compd 1007 (2024) 176497.
[167] L. Liu, et al., J. Magnes. Alloy. 9 (6) (2021) 1906–1921.
[168] R. Pandey, et al., J Alloy Compd 770 (2019) 473–482.
[169] Z. Xu, et al., J. Magnes. Alloy. 11 (10) (2023) 3800–3814.
[170] Y. Gu, et al., Mater. Corros. (76) (2025) 996–1009.
[171] J. Xue, et al., Adv. Eng. Mater. 25 (21) (2023) 2300620.
[172] J. Jiao, et al., Acta Metall. Sin. (Engl. Lett.) 37 (3) (2024) 484–498.
[173] K. Dong, et al., Electrochim. Acta 462 (2023) 142662.
[174] L. Coelho, et al., Surf Interfaces 16 (2019) 15–21.